

Alma Mater Studiorum Università di Bologna  
Archivio istituzionale della ricerca

Complexity of graphite formation in response to metamorphic methane generation and transformation in an orogenic ultramafic body

This is the final peer-reviewed author's accepted manuscript (postprint) of the following publication:

*Published Version:*

Boutier, A., Martinez, I., Sissmann, O., Agostini, S., Daniel, I., Van Baalen, M., et al. (2024). Complexity of graphite formation in response to metamorphic methane generation and transformation in an orogenic ultramafic body. *GEOCHIMICA ET COSMOCHIMICA ACTA*, 364, 166-183 [10.1016/j.gca.2023.10.028].

*Availability:*

This version is available at: <https://hdl.handle.net/11585/955194> since: 2024-02-01

*Published:*

DOI: <http://doi.org/10.1016/j.gca.2023.10.028>

*Terms of use:*

Some rights reserved. The terms and conditions for the reuse of this version of the manuscript are specified in the publishing policy. For all terms of use and more information see the publisher's website.

This item was downloaded from IRIS Università di Bologna (<https://cris.unibo.it/>).  
When citing, please refer to the published version.

(Article begins on next page)

Complexity of graphite formation in response to metamorphic methane generation and transformation in an orogenic ultramafic body

Antoine Boutier<sup>1,2,3</sup>, Isabelle Martinez<sup>2</sup>, Olivier Sissmann<sup>4</sup>, Samuele Agostini<sup>5</sup>, Isabelle Daniel<sup>3</sup>, Mark Van Baalen<sup>6</sup>, Sara Mana<sup>7</sup>, Alberto Vitale Brovarone<sup>8,9,5\*</sup>

\*Corresponding author

<sup>1</sup>*Dipartimento di Scienze della Terra, Università degli Studi di Torino, Via Valperga Caluso 35, 10100 Torino, Italy, ORCID: 0000-0003-4013-0566*

<sup>2</sup>*Institut de Physique du Globe de Paris, Sorbonne Paris Cité, Université Paris Diderot, UMR 7154 CNRS, 1 rue Jussieu, F-75005 Paris, France*

<sup>3</sup>*Université Claude Bernard Lyon 1, LGL-TPE, CNRS, ENS de Lyon, Université Jean Monnet Saint-Etienne UMR 5276, Villeurbanne, 69622, France*

<sup>4</sup>*IFP Energies Nouvelles, Rueil-Malmaison Cedex, France*

<sup>5</sup>*Institute of Geosciences and Earth Resources, National Research Council of Italy, Pisa, Italy*

<sup>6</sup>*Harvard University, EPS Dept., 20 Oxford St., Cambridge, MA 02138*

<sup>7</sup>*Department of Geological Sciences, Salem State University, Salem, MA 01970, USA*

<sup>8</sup>*Dipartimento di Scienze biologiche, geologiche e ambientali, Via Zamboni, 67, Bologna, Italy*

*<sup>9</sup>Institut de Minéralogie, de Physique des Matériaux et de Cosmochimie (IMPMC),  
Sorbonne Université, Muséum National d'Histoire Naturelle, UMR CNRS 7590, IRD  
UR206, 75005 Paris, France*

## Abstract

The fate of carbon in subduction is explored by considering fluid-rock interactions in a body of metamorphosed ultramafic rocks from the Appalachian belt as potential proxies for metasomatism and carbon recycling (e.g., infiltration, solution, precipitation) in the mantle wedge at convergent margins. Ultramafic rocks may record intense redox variations affecting the exchanges between solid and fluid carbon-bearing phases. The Belvidere Mountain Complex (BMC) in Vermont, USA is an ultramafic body that underwent Ordovician Taconic subduction metamorphism up to 510-520 °C and 0.9-1.3 GPa. Previous investigations indicate that the BMC experienced partial serpentinization and carbon recycling in the subduction zone. Here bulk  $\delta^{11}\text{B}$ ,  $\text{Sr}^{87}/\text{Sr}^{86}$  and  $\delta^{13}\text{C}$ , data, in-situ microRaman spectroscopy and bulk  $\delta^{13}\text{C}_{\text{CH}_4}$  and  $\delta^2\text{H}_{\text{CH}_4}$  on fluid inclusions, and numerical modeling results aim to constrain the origin and formation mechanisms of carbon-bearing solid and fluid phases in the BMC. Bulk  $^{87}\text{Sr}/^{86}\text{Sr}$  ratios and  $\delta^{11}\text{B}$  of the BMC rocks suggest infiltration of metasediment-derived fluids inside the mafic/ultramafic body. Carbonates present in the studied ultramafic and mafic rocks have  $\delta^{13}\text{C}$  values ranging from -7.26 to -1.27‰. This range was found to record progressive reduction of an initial isotopically light carbonate to methane under reducing conditions. MicroRaman spectroscopy on fluid inclusions confirms  $\text{CH}_4$ -rich gaseous compositions, along with  $\text{N}_2$ ,  $\text{NH}_3$ , and S-H compounds, which support a metasedimentary origin for the fluid infiltrating the BMC. Methane-rich

fluid inclusions were observed in partially serpentinized peridotites, in carbonate veins, and in amphibolite bodies associated with the ultramafic body, and as well in the surrounding metasedimentary rock units. The  $\delta^{13}\text{C}$  and  $\delta^2\text{H}$  of methane in fluid inclusions show a wide range of values in ultramafic rocks from -45.2‰ to -12.6‰ for carbon and -226‰ to -140‰ for hydrogen. The methane stable isotope data suggest the presence of two types of methane preserved in studied samples, formed by high-temperature thermogenic processes of metamorphosed graphitic carbon and by abiotic conversion of more oxidized carbon bearing species in the presence of  $\text{H}_2$ -rich fluids produced during metamorphic serpentinization. The BMC also hosts a remarkable example of graphite deposit, with up to 3.90 wt% graphite, along a ~6 m-thick zone within the serpentinized ultramafic body and along lithologic contacts. The  $\delta^{13}\text{C}$  composition of the graphite clusters at -15‰ (VPBD), which is consistent with the composition of graphite precipitating from the mixing of the two types of methane-bearing fluids identified in fluid inclusions. The mixing between metasediment-derived and serpentinization-related methane-rich fluids is proposed as the mechanism leading to graphite precipitation. Further complexity is suggested by carbonate reduction evidenced in the samples, which may have locally contributed to the formation of graphite on the precursor carbonate domains. The BMC rocks highlight the variability of carbon recycling processes, including carbon mobilization from multiple solid sources, and mixing of multiple carbon-bearing fluids in a dynamic fluid-rock system, with carbon mobilization and sink adapting to evolving redox conditions.

Keywords: Abiotic methane; C fluxes at subductions zones; Natural graphite; Isotopes; Belvidere Mountain Complex

## 69 1 Introduction

70 Subduction is a major actor in the cycling of carbon between surface and deep  
71 reservoirs. As material is brought down along the subducted slab, fluid release and  
72 interaction with the overlying mantle wedge creates complex pathways for element  
73 mobility as well as fluid intake and outtake (Dasgupta, 2013; Dasgupta and  
74 Hirschmann, 2010; Manning, 2014). Metamorphic reactions along the subduction path  
75 can regulate element mobility as well as fluid speciation (e.g, Evans, 2012; Hayes and  
76 Waldbauer, 2006). Carbon in subduction zone rocks can be present under different  
77 valence states, from -4 to +4, in various forms, such as carbonate, organic matter, and  
78 several fluid species such as CO<sub>2</sub>, CH<sub>4</sub>, as well as many others (e.g. Manning et al.,  
79 2013; Sverjensky et al., 2020). Carbon mobilization in subduction zones is known to  
80 produce different carbonic fluids: CO<sub>2</sub>-rich fluids resulting from decarbonation  
81 reactions (Gorman et al., 2006; Kerrick and Connolly, 1998, 2001a, 2001b; Stewart et  
82 al., 2019), carbonate dissolution (e.g., Ague and Nicolescu, 2014; Facq et al., 2014;  
83 Frezzotti et al., 2011; Piccoli et al., 2021), CH<sub>4</sub>-rich fluids from serpentinization of  
84 preserved peridotite in the slab and of the overlying mantle wedge (Boutier et al., 2021;  
85 Peng et al., 2021; Vitale Brovarone et al., 2020a, 2017) or from organic matter-rich  
86 metasedimentary rocks (Clift, 2017; Tumiati et al., 2020; Vitale Brovarone et al.,  
87 2020b) and mantle derived CO<sub>2</sub>/CH<sub>4</sub> fluids (Dasgupta, 2013 and references therein;  
88 Green et al., 1987). The precipitation of carbon-bearing minerals, most notably  
89 carbonates, graphite, and diamond, as well as other compounds is largely related to  
90 the transformation of these fluids during the percolation through crustal and mantle  
91 rocks. The interplay and interrelations among processes of carbon mobilization and  
92 precipitation –hereafter carbon recycling– at subduction zones are central in the

evolution of Earth and life, and also to assess the potential habitability of other celestial bodies where subduction is or was once active (Giovannelli et al., 2022). The formation and migration of CH<sub>4</sub> and associated reduced fluid species –most notably H<sub>2</sub>– is of particular interest in the study of how life emerged on Earth and potentially elsewhere, and how deep it could extend in the subsurface biosphere (Colman et al., 2017; Gold, 1992; Ménez et al., 2018; Plümper et al., 2017; Schrenk et al., 2013).

The fate of metamorphic methane in subduction is strongly dependent upon multiple fluid-rock interactions that may take place in slab and mantle wedge forming rocks. For instance, prograde metamorphism of organic-rich metapelitic rocks may release aqueous fluids rich in CH<sub>4</sub>, migration of which may favor the reactivity of more oxidized carbonate-rich rocks and the precipitation of graphite along lithologic boundaries (Evans et al., 2002). Or, reducing fluids derived from ultramafic or mafic rocks may lead to the reduction of carbonate minerals, the formation of abiotic methane, and/or the precipitation of graphite (Galvez et al., 2013; Tao et al., 2018; Vitale Brovarone et al., 2017). Ultimately, the migration of metamorphic methane may support metabolic reactions in the deep subsurface biosphere (Vitale Brovarone et al., 2020a). However, field examples recording interaction of reduced carbon-rich fluids remain insufficient to understand the fate of metamorphic methane at depth. Here we present results from the Belvidere Mountain complex (BMC). The BMC consists of an ultramafic/mafic body that has been interpreted as a fragment of the Iapetus ocean that was involved in the Taconic orogeny and that recorded HP metamorphism during the Ordovician (Chew and van Staal, 2014; Gale, 1980; Honsberger et al., 2017). This locality hosts a remarkable example of metamorphic methane formation and migration and fluid-mediated graphite deposition in a subduction zone. This work integrates field, microstructural, fluid inclusion, major and trace element and isotopic geochemical data

to investigate the mechanisms of metamorphic methane formation, migration, and transformation in a subduction setting.

## 2 Geologic settings

The Belvidere Mountain Complex (BMC) is a body of mafic/ultramafic rocks located in Northern Vermont and belonging to the Appalachian Mountain system. The complex has been interpreted as a remnant of an ocean-continent transition zone associated with the extension of the Laurentian margin that underwent peak blueschist-facies metamorphism during the Ordovician Taconic subduction (Chew and van Staal, 2014; Gale, 1980). It exhibits variably serpentinized peridotites, mainly dunite and harzburgite, associated with metabasic and metafelsic rocks. The BMC is tectonically embedded within Proterozoic to Cambrian metasedimentary and metavolcanic formations (Fig. 1). Taconic age, peak blueschist-facies metamorphic conditions of the BMC are constrained at 0.9-1.3 GPa and 510-520 °C in metabasic rocks (Honsberger et al., 2017; Laird et al., 1993). A recent study provides additional insight on the PT path of the massif with evidence of mineral assemblages stable at ~1.65–2.0 GPa and ~450–480 °C, and ~1.0–1.4 GPa and ~515–550 °C (Honsberger, 2023). The rocks preserve features of interactions with aqueous fluids and in the subduction zone, leading to variable serpentinization (10-100 vol% serpentine) (Boutier et al., 2021; Labotka and Albee, 1979). This tectonometamorphic event was dated at 505-473 Ma by  $^{40}\text{Ar}/^{39}\text{Ar}$  amphibole and mica geochronology (Castonguay et al., 2012; Laird et al., 1993).

### 3 Methods

MicroRaman spectroscopy of minerals and fluid inclusions was performed at the Department of Earth Sciences, University of Turin, with a LabRAM HR (VIS) (HORIBA Jobin Yvon) equipped with a 532.11 nm, solid-state Nd laser, a Super Notch Plus filter with a grating of 600 grooves/mm leading to a spectral resolution of  $1\text{ cm}^{-1}$ . The laser emission power was set at 80 mW and focused to  $5\text{ }\mu\text{m}$  with a 100x objective with a laser power on the sample  $< 5\text{ mW}$ . Calibration was performed using the  $520.6\text{ cm}^{-1}$  band of a silicon standard for the  $100\text{--}2000\text{ cm}^{-1}$  range, and the  $2331\text{ cm}^{-1}$  band of atmospheric  $\text{N}_2$  for the  $2000\text{--}4000\text{ cm}^{-1}$  range. Four accumulations of 30–60 s were collected for each spectrum. Raman spectra of fluid inclusions were performed on double-polished thick sections.

Scanning electron microscopy (SEM) imaging and energy-dispersive X-ray spectroscopy (EDS) compositional analyses were carried out using a Zeiss EVO15 equipped with a LaB6 source, a high-definition backscattered electron detector (HDBSE), and an Oxford Instruments UltimMax 100 detector at the Deep Carbon Lab, (Department of Biological, Geological, and Environmental Sciences, University of Bologna). Additional analyses were performed with a tungsten (W) SEM-JEOL JSM-IT300LV Scanning Electron Microscope combined with an energy dispersive spectrometry (EDS) Energy 200 system and an SDD X-Act3 detector (Oxford Inca Energy) at the Department of Earth Sciences of Turin University. Data were processed with the AztecLive and INCA softwares from Oxford Instruments. Semi-quantitative analysis employed 15kV accelerating voltage and a beam current of 50 nA and 20 s to 40 s counting total time. Natural and synthetic mineral and oxide standards were employed. EDS calibration was made using Cobalt standard.



Quantitative wavelength-dispersive spectrometer (WDS) analyses were carried out using a JEOL 8200 Super Probe with a W source at the Department of Earth Sciences “Ardito Desio” of Milan University. The microprobe operating settings under maximum emission peak were 15kV accelerating voltage under 5 nA, beam diameter 1  $\mu$ m, counting time 30 s, and background counting time 10 s. Sixteen oxide compositions were measured, using synthetic and natural standards: grossular (Si, Al and Ca), omphacite (Na), K-feldspar (K), fayalite (Fe), forsterite (Mg), rhodonite (Mn), niccolite (Ni), ilmenite (Ti), galena (Pb and S), pure Cr, pure Zn and pure Cu.

Portions of samples were cut to remove weathered and surface organic contamination, and then crushed and pulverized with Plattner’s steel and agate mortars. Considering the very high amount of graphite, the potential effect of organic contaminations by groundwater circulation was considered negligible. Analyses of total organic carbon (TOC) were performed on aliquots of about 1 g of dried, decarbonated samples (HCl, 6 mol/L, attacked at ambient temperature for one night) using a Flash EA1112 elemental analyzer coupled to a Thermo Finnigan DELTA plus XP isotope ratio mass spectrometer via a ConFlo IV interface at IPGP, Paris. Aliquots of the companion, non-decarbonated sample were also analyzed for Total Inorganic Carbon (TIC)+ Total inorganic carbon (TOC). Graphitic C concentrations in samples presented herein correspond to the TOC.

The  $\delta^{13}\text{C}$  and the  $\delta^{18}\text{O}$  of carbonate were obtained at the Institute of Geosciences and Earth Resources, Pisa, on a GasBench II with a continuous-flow IRMS setup, after the method of Breitenbach and Bernasconi, (2011). Isotope ratios are reported in permil (‰) using the conventional  $\delta$ -notation and with respect to the Vienna Stanard Mean

187 Ocean Water (V-SMOW) for oxygen and Vienna Pee Dee Belemnite (V-PDB) for  
188 carbon. Standard deviation was 0.05‰ for both  $\delta^{13}\text{C}$  and  $\delta^{18}\text{O}$ .

189 The  $\delta^{13}\text{C}$  and  $\delta^2\text{H}$  of  $\text{CH}_4$  was obtained at IFP energies nouvelles by extracting the  
190 gas by crushing inclusion-rich samples in a sealed modified planetary mill. The  
191 samples were placed in a ZrO jar and sealed by an inlet/outlet-equipped cover. The  
192 jar was flushed with  $\text{N}_2$  for around 60 seconds, then sealed and crushed at 700 rpm  
193 for 240 seconds. The gas was then extracted from the jar by connecting vacuum  
194 Exetainer® sample vials. Three vials were collected for each sample. The  $\delta^{13}\text{C}$  of each  
195 sample was measured by two independent techniques: the first vial of each sample  
196 was injected in triplicate in a Picarro G2210-i Isotope Analyzer, to obtain the  $\delta^{13}\text{C}$  of  
197  $\text{CH}_4$  and the C1/C2 ratio. The two other vials were used to analyze  $\delta^2\text{H}$  and  $\delta^{13}\text{C}$  of  
198  $\text{CH}_4$  with a GC-MS, respectively. Analyses by GC-MS were calibrated using two  
199 internal gas standards.

200 Bulk  $\delta^{11}\text{B}$  was analyzed at IGG-CNR, Pisa; for each sample ~0.2 g of sample powder  
201 was treated by alkaline fusion in platinum crucibles with a 4:1 flux to sample ratio.  
202 Boron was then extracted from the fusion cakes by repeated crushing and centrifuging  
203 of the cakes in high pH B-free water. It was further purified by passing the solution  
204 through anion and cation exchange columns. Anion columns were packed with  
205 Amberlite IRA-743 boron-specific anion exchange resin, while cation-exchange  
206 columns were packed with AG 50W-X8 resin. The procedure used an anion column  
207 step, followed by a cation column step and then a final (repeat) anion column step to  
208 produce the final purified boron solution, as described by (Agostini et al., 2021). Boron  
209 isotopic compositions were measured on a Thermo Scientific™ Neptune series multi-  
210 collector (MC)-ICP-MS in Pisa, specially tuned for  $^{11}\text{B}/^{10}\text{B}$  analysis, following Foster,  
211 (2008). Samples were diluted to contain ~20 ppb B and were then bracketed with NBS

212 951 boric acid standard solution of the same concentration, to correct for instrument-  
213 induced mass fractionation. A detailed description of analytical procedure, along with  
214 accuracy of several analyses of NIST SRM 951 and other international and in-house  
215 standards is available in (Agostini et al., 2021).

216 Strontium isotope analyses were performed using a Thermo Fisher Scientific Neptune  
217 Plus MC-ICP-MS at IGG-CNR of Pisa as described in detail in [Agostini et al. \(2022\)](#).  
218 After sample powder digestion in concentrated HF+HNO<sub>3</sub>, strontium was extracted  
219 from matrix in a class 100 clean room by ion-exchange purification through Sr-spec  
220 resin Strontium analyses were performed in 2% HNO<sub>3</sub> solution containing 100-200  
221 ng\*g<sup>-1</sup> of analyte. Values are corrected for <sup>87</sup>Sr/<sup>86</sup>Sr of NBS 987 =0.710248.

222 Whole-rock analyses were performed at the Service d'Analyse des Roches et  
223 Minéraux (SARM, Centre de Recherches Pétrographiques et Géochimiques, Nancy,  
224 France) by alkali fusion of rock samples (LiBO<sub>2</sub>), followed by concentration  
225 measurements using an ICP-OES iCAP 6500 (Thermoscientific) for major elements,  
226 and an ICP-MS X7 (Thermoscientific) for minor elements (protocol by Carignan et al.,  
227 2001). See Supplementary Materials 1 for details on uncertainties and detection limits.

228 Numerical modeling of isotopic fractionation was done with Rayleigh and batch  
229 equations and fractionation factors from Bottinga (1969) using Python.  
230 Thermodynamic modeling of COH fluid and associated carbon solid was done using  
231 equations from Huizenga (2005) to track the carbon activity using a python code. Both  
232 models were coupled to investigate and model the interaction of the various COH  
233 fluids.

## 4 Results

### 4.1 Field relationships

Figure 2 and Table 1 show the location and main features of the selected samples. Besides samples of variably serpentinized peridotites, rodingites, and surrounding metasedimentary rocks, the most important samples presented in this study were collected from two main outcrops, graphite zone A and B hereafter, showing evidence of graphite precipitation. Graphite zone A consists of a vertical, ~6 m thick graphite-rich shear zone cutting through the ultramafic body (Fig. 2A). This is the locality first described in Kerper et al. (2008). Graphite zone A is separated from the enclosing serpentinized peridotite by a rather sharp boundary (Fig. 2B). However, the host serpentinite next to the graphite zone selvages appears variably carbonated. The carbonation is present as veins, mainly on the East side of the graphite zone, and micro-scale pervasive carbonation is visible on both sides of the graphite zone (Fig. 2C). The second outcrop, referred to as graphite zone B is located along the contact between the BMC serpentinized peridotites and amphibolites (Fig. 2D). The outcrop forms a vertical wall making the boundary with the adjacent amphibolite. The amphibolite next to the contact shows evidence of fluid circulation and metasomatism, as indicated by the presence of cross-cutting veins (mainly albite, carbonate, and graphite; Fig. 2E) and local rodingitization (mainly tremolite, garnet, epidote, carbonate; Fig. 2F).

Samples V18-1a,c,e correspond to metasedimentary rock of the carbonaceous Ottauquechee Formation, from an outcrop located in Hyde Park, Vermont 20 km south of the BMC. Sample V18-1a consists of fine-grained muscovite, quartz, chlorite, abundant organic matter, and other opaque minerals. Sample V18-1c is quartz-richer, and contains muscovite, chlorite, minor organic matter, coarse-grained isolated and

locally disseminated carbonate, coarse-grained sulfides, and detrital zircons. Samples V18-2a,b, V18-3a,b and V18-11 (Fig. 3) consist of slightly serpentinized peridotites. Samples V18-5(a-i), V18-7a,c, and V18-Y(1,b) are from graphite zone A. Samples V18-6a,d, V18-8, V18-9, and V18-10 are variably carbonated serpentinites from the selvage of graphite zone A. Samples V18-12 to V18-15 are from graphite zone B and correspond to variably metasomatized amphibolites and cross-cutting veins. Sample V18-4 is a graphite-carbonate-bearing rodingite.

## 4.2 Petrographic features

Although the petrologic features of the BMC serpentinized peridotites and related mafic rocks have been treated in the literature (Boutier et al., 2021; Labotka and Albee, 1979; Laird et al., 2001), the associated graphite mineralization remains poorly investigated (Carlsen et al., 2015; Chidester et al., 1978; Kerper et al., 2008; Van Baalen et al., 2009). Kerper et al. (2008) described this graphite mineralization and proposed that it was due to fluid mixing between external fluids from underlying carbonaceous metasediments and internal methane-rich fluids within the serpentinite. However, they could not assess the origin of the methane-rich fluids. Here, the main features of graphite zones A and B are presented. Details on samples V18-2a,b, V18-3 and V18-4 (rodingites) can be found in Boutier et al. (2021). The sample series V18-5a to 5i corresponds to a high-resolution transect across graphite zone A (Fig. 4). The outcrop comprises two main lithologies, namely tremolite-chlorite-graphite-rich rocks located at the center of the zone (samples V18-5c,d), and antigorite-graphite-rich rocks located at the selvages (samples V18-5a,b,e,f,g,h,i). Carbonate is present at the edge of the graphite zone as discordant veins (sample V18-5a), or in the matrix of both antigorite-graphite rocks (V18-5i, Fig. 5A). Samples V18-7a,c display graphite associated to carbonate. Samples V18-6(a,d), V18-8, V18-9, and V18-10 have

284 disseminated carbonate-veins and do not contain graphite. Samples V18-Y1 and V18-  
285 Yb are two loose blocks collected at the base of the graphite zone showing  
286 complementary features, possibly reflecting the early stages of fluid/rock interaction.

287 V18-5c and V18-5d correspond to samples at the center of graphite zone A. They  
288 consist of tremolite (up to 200 $\mu$ m long), antigorite, chlorite, and graphite, and show  
289 complex deformation features (Fig. 5B). Graphite is present in the matrix forming  
290 coronas around tremolite crystals. Microstructural relationships indicate that at least  
291 some of the antigorite present in these samples formed at the expense of former  
292 tremolite (Fig. 5B).

293 Sample V18-5a is composed of antigorite and graphite with discordant carbonate  
294 veins (Fig. 5C). However, the former presence of tremolite is clearly indicated by the  
295 pseudomorphic growth of antigorite aggregates on euhedral amphibole crystals (Fig.  
296 5C). By comparison with samples V18-5c,d, the microstructures suggest that the  
297 graphite rims surrounding these pseudomorphoses formed prior to the replacement of  
298 tremolite by antigorite. The graphite deposit coincides with the deformation  
299 experienced along the graphite zone A. Similar pseudomorphic microstructure and  
300 deformation can be observed in other antigorite samples from V18-5e-i.

301 Sample V18-7c corresponds to a metasomatized serpentinite to the East of graphite  
302 zone A, and consists of antigorite, dolomite, calcite, brucite, and graphite. SEM-based  
303 BSE imaging suggests at least local conversion of dolomite into calcite, brucite, and  
304 graphite (Fig. 5D). This microstructure, however, was not observed in any of the other  
305 studied samples.

306 V18-Y1 has a breccia-like structure and consists of clasts of antigorite in a matrix of  
307 fine-grained foliated tremolite. Post-kinematic diopside porphyroblasts partially

308 overgrew the foliated tremolite matrix and, to minor extent, the serpentine clasts (Fig.  
309 5E). This sample does not contain graphite.

310 V18-Yb shares mineralogic features of V18-Y1 with clasts of antigorite or tremolite  
311 aggregates in a matrix of fine-grained tremolite (Fig. 5F). Also, in this case,  
312 microstructures suggest that at least a part of the antigorite present in the rock formed  
313 after the former tremolite. Graphite is abundant in the rock. It is disseminated in the  
314 fine-grained tremolite matrix, and forms aggregates around larger tremolite crystals or  
315 antigorite aggregates in the clasts.

316 Six samples were collected from the graphite zone B (samples V18-12a,b,c, V18-  
317 13a,b, V18-14 and V18-15). Samples V18-12a and V18-12c have structures and  
318 mineral assemblages similar to samples V18-5c and v18-5d of graphite zone A, with  
319 tremolite crystals up to ~200  $\mu\text{m}$  long in a matrix of chlorite (Fig. 6A). Graphite is  
320 abundant in the matrix and forms coronas around the tremolite crystals (Fig. 6A).

321 Samples V18-12c, V18-13a, V18-13b, V18-14, and V18-15 are mainly composed of  
322 brown amphibole – partially to largely replaced by green amphibole –, epidote, and  
323 titanite, in agreement with previous description of variably retrogressed amphibolite-  
324 facies mafic rocks in the BMC (Labotka and Albee, 1979). In addition, graphite was  
325 found as inclusions along the outer rim of epidote and titanite (Fig. 6B). As observed  
326 in graphite zone A, field and microstructural relationships indicate that the rock  
327 recorded fluid overpressure events indicated by crosscutting veins composed of albite,  
328 brown mica, carbonate, and graphite (Figs. 2E and 6C). The presence of carbonate  
329 along albite-hosted hydrofractures suggests that the carbonate post-dated the  
330 formation of the albite veins. Microstructures also suggest that graphite formed by  
331 transformation of the vein-filling carbonate rather than coprecipitating with it (Fig. 6D).

This is suggested by the preferential distribution of graphite along pressure-solution domains (Fig. 6C,D). The presence of secondary, CH<sub>4</sub>-rich fluid inclusions was identified in carbonate minerals by MicroRaman spectroscopy.

Samples V18-12c, V18-13a, V18-13b, V18-14, and V18-15 are mainly composed of hornblende, epidote, titanite, and albite-carbonate veins, consistent with the BMC amphibolite (Labotka and Albee, 1979), but show evidence of fluid infiltration as indicated by the presence of graphite and carbonate formed along grain boundaries or micro-cracks. Particularly V18-15 contains large amounts of carbonate featuring methane-rich fluid inclusions.

#### 4.3 Fluid inclusions analysis

Boutier et al., (2021) described the presence of secondary fluid inclusions containing CH<sub>4</sub>, N<sub>2</sub>, NH<sub>3</sub> and S-H/H<sub>2</sub>S in olivine from sample V18-2a in the BMC ultramafic rocks. These reduced fluids were interpreted to have formed through the process of high-pressure serpentinization. Here we provide additional MicroRaman data on fluid inclusions from several other samples from the BMC, and more precisely in olivine from a another weakly serpentinized peridotite (V18-11), in vein calcite (V18-4 and V18-6d), in titanite, plagioclase, and carbonate from amphibolites (V18-12c and V18-14), and in quartz from nearby metasedimentary formations (V18-1b).

The fluid inclusion speciation as derived from MicroRaman spectra analysis is presented in Figure 3. MicroRaman spectra (Supplementary Materials 2) show the presence of marked CH<sub>4</sub> bands (2912 cm<sup>-1</sup>), as well as N<sub>2</sub> (2327 cm<sup>-1</sup>), NH<sub>3</sub> (3324 cm<sup>-1</sup>), and S-H/H<sub>2</sub>S (2575 cm<sup>-1</sup>). This water-free fluid inclusion composition was found in olivine from partially serpentinized peridotites and in calcite from the graphite zone A. The proportion of CH<sub>4</sub> is dominant in olivine-hosted inclusions and decreases in



carbonate-hosted inclusions. Olivine-hosted fluid inclusions contain step-daughter hydrous solid phases such as lizardite and brucite, indicating that the initial fluid trapped in the olivine was aqueous. In graphite zone B, calcite-hosted inclusions show similar compositions, whereas plagioclase and titanite-hosted inclusions are water-dominated with less abundant CH<sub>4</sub> and N<sub>2</sub>.

In Boutier et al. (2021) we stated that antigorite and chrysotile were the only serpentine polysomes present in the BMC rocks. However, complementary observations in sample V18-2a reveal the presence of veins of lizardite, in particular, brownish lizardite veins that had been misinterpreted as antigorite. The presence of lizardite-vein in only a few samples is not associated with compositional changes in fluid inclusion, Supplementary material 2 shows olivine-hosted inclusions composition for V18-11 similar to the composition for V18-2a presented in Boutier et al. (2021). Therefore, we conclude that this feature does not substantially affect our interpretations of the metamorphic origin of the CH<sub>4</sub>-bearing fluid inclusions and their most plausible formation at antigorite-facies conditions as proposed in Boutier et al. (2021). The chronological relationships between antigorite and lizardite in sample V18-2a are not obvious, which possibly suggests conditions close to the antigorite-lizardite transition (380-400 °C, Schwartz et al., 2013).

#### 4.4 Bulk rocks trace and major elements compositions

Major elements of the BMC ultramafic rocks show that the least serpentinized samples of the BMC (V18-2a,b) share MgO vs Al<sub>2</sub>O<sub>3</sub> compositions with both abyssal and orogenic/ophiolitic peridotites (Fumagalli and Klemme, 2015). Tremolite-rich samples located at the center of the graphite zone A display a decrease of SiO<sub>2</sub> and MgO content, and an increase of Al<sub>2</sub>O<sub>3</sub> and CaO content with respect to the surrounding ultramafic rocks. Samples most affected by graphite zone B (V18-12b) display a

decrease of  $\text{Al}_2\text{O}_3$ ,  $\text{Fe}_2\text{O}_3$  and an increase of  $\text{SiO}$  and  $\text{MgO}$  in respect to the less or unaffected mafic rocks (V18-12c, V18-14, V18-15). The major element composition of the samples less affected by the graphite zone B are in range of the mafic rocks composition presented in Spandler et al. (2003).

Chondrite-normalized Rare-Earth Element (REE) spider diagrams of the studied samples along with major elements data are presented in Supplementary material 3. Sample V18-1a has a positive REE slope, i.e.,  $\text{La}_N > \text{Lu}_N$ , consistent with terrigenous sedimentary rocks (Ague, 2017; Spandler et al., 2003). Samples of BMC variably serpentinized peridotites (V18-2a,b, V18-3a, V18-5b,c,d,g,h,i, V18-7a, V18-8, V18-10) have very low REE concentrations and patterns consistent with serpentinized ultramafic rocks (Deschamps et al., 2013). Samples from graphite zone A (V18-5a-i) and highly rich in graphite (V18-7c) have REE patterns similar to the variably serpentinized peridotites. Samples from amphibolite and from graphite zone B show patterns typical of gabbro, with the Eu positive anomaly attributed to preferential incorporation in plagioclase (Philpotts and Schnetzler, 1968). REE spectra indicate that the protolith of graphite zone A and B corresponds to depleted and differentiated mantle, respectively.

#### 4.5 Carbon content and isotopy

Total organic carbon (TOC) content is presented in Table 1. The complete details including standard deviation are available in Supplementary material 4. Slightly serpentinized peridotite and serpentinized rocks have TOC content of 0.001-0.02 wt. %. These values correspond to the range of TOC contents in ultramafic rocks from Northern Apennines and ODP samples (>0.1% to 0.7%) (Schwarzenbach et al., 2013). The TOC content of graphite zone A rocks ranges between 1.02 and 3.90 wt. %,

405 showing a peak of TOC in samples close to the center of the shear zone (samples  
406 V18-5g and V18-5f). This peak of TOC content is not correlated with the observed the  
407 presence or not of tremolite within this graphite zone (see Section 4.1).

408 The TOC content of graphite zone B ranges from 0.2 to 3.69 wt.% (Table 1). These  
409 values are higher relative to the TOC content ( $>0.1$  wt%) of mid-ocean ridge crustal  
410 rocks and their metamorphic equivalents (Schwarzenbach et al., 2013; Shilobreeva et  
411 al., 2011).

412 The TOC contents of samples V18-1a,c,e from the Ottawuechee formation range  
413 from 0.17 wt% to 1.99 wt.% and are consistent with the range of TOC contents of black  
414 schists (Peltola, 1968; Zhang et al., 2018).

415 Isotopic analyses of  $\delta^{13}\text{C}_{\text{org}}$  were conducted to investigate the processes of graphite  
416 deposition and its carbon sources.  $\delta^{13}\text{C}_{\text{org}}$  data are presented in Table 1 and Figure 7,  
417 with uncertainties corresponding to the standard deviation. Samples from the  
418 Ottawuechee formation (V18-1a-e) exhibit an average  $\delta^{13}\text{C}_{\text{org}}$  value of  $-25.1$  ‰  
419 ( $\pm 0.2$ ‰;  $n=3$ ). These values are consistent with the  $\delta^{13}\text{C}_{\text{org}}$  signature of chlorite-biotite  
420 zone metapelitic rocks unaffected by fluid-rock interactions from the Appalachian belt  
421 (Cook-Kollars et al., 2014; Zhang et al., 2018). The average  $\delta^{13}\text{C}_{\text{org}}$  of least  
422 serpentinized peridotites is  $-27.9$  ‰ ( $\pm 0.4$ ‰;  $n=5$ ), which is consistent with the  
423 signature of serpentinized peridotites of oceanic affinity (Schwarzenbach et al., 2013).  
424 However, it corresponds to a relatively low amount of carbon ( $< 0.03$  wt%) and could  
425 be attributed to recent or biological contamination, as  $\delta^{13}\text{C}$  of C3 photosynthesis range  
426 around  $-28$  ‰. The  $\delta^{13}\text{C}_{\text{org}}$  values of samples from graphite zone A and B are  
427 comparable and correspond to  $-15.9$  ‰ ( $\pm 1$ ‰;  $n=9$ ) and  $-15.2$  ‰ ( $\pm 1.2$ ‰;  $n=3$ ),  
428 respectively. These values are clearly different from the  $\delta^{13}\text{C}_{\text{org}}$  signature of regular

429 ultramafic rocks of the BMC. The value of graphite-poor serpentinite located close to  
430 graphite zone A ranges from  $-29.5$  to  $-20.2$  ‰ (Table 1). A graphite-bearing  
431 amphibolite next to graphite zone B has a  $\delta^{13}\text{C}_{\text{org}}$  value of  $-20.5$  ‰ (Table 1).

432 The  $\delta^{13}\text{C}_{\text{org}}$  values of serpentinites around the graphite zone A show disparity which  
433 could correspond to the influence of the graphite zone A. The  $\delta^{13}\text{C}_{\text{org}}$  of the samples  
434 are not correlated to the direct proximity to the graphite zone A, as the samples directly  
435 located near it, such as V18-6a ( $\delta^{13}\text{C} = -28.6$  ‰), do not exhibit  $\delta^{13}\text{C}_{\text{org}}$  value close to  
436 the graphite zone A ( $\delta^{13}\text{C} = -15.9$ ). However, the TOC content indicates a correlation  
437 with the graphite zones (Fig. 8A), showing that samples with increasing TOC content  
438 have values closer to that of the graphite zone A and B. Both samples from the  
439 graphite veins in the ultramafic body and the amphibolite contact show  $\delta^{13}\text{C}$  signature  
440 centered around  $-15$  ‰ and is homogeneous, indicating a common source for graphite  
441 zone A and B. However, the variation of the  $\delta^{13}\text{C}$  inside the graphite veins appears  
442 uncorrelated to the TOC content of the samples (Fig. (8A), as samples with similar  
443 TOC content range from  $-17.7$  ‰ to  $-13.6$  ‰.

444 Carbonates (inorganic carbon) present as veins, associated with serpentine, or in  
445 rodingites exhibit a  $\delta^{13}\text{C}_{\text{inorg}}$  signature ranging from  $-6.49$  to  $-1.27$  ‰ (Table 1 and Fig.  
446 7). The carbonate in altered amphibolite V18-14 has a value of  $-7.62$  ‰. These values  
447 are lower relative to the average signature of carbonate in metamorphic carbonated  
448 ultramafic rocks (Collins et al., 2015), with the exception of rocks with low  
449 carbonate/silicate ratios and affected by  $\text{CO}_2$ -producing metamorphic decarbonation  
450 reactions or fluid-deposited carbonates derived from infiltration of fluids sourced from  
451 OC-bearing metasedimentary rocks (Bebout, 1991; Bebout and Barton, 1993;  
452 Scambelluri et al., 2016). Additional interpretations are discussed in Section 5.2. The

oxygen isotopic composition  $\delta^{18}\text{O}$  of carbonate relative to the SMOW ranges from 8.91 to 16.64 ‰ (Fig. 9). These values are consistent with  $\delta^{18}\text{O}$  of carbonate in ultramafic rocks metamorphosed to blueschist-facies conditions (Collins et al., 2015). However, the carbonate  $\delta^{18}\text{O}$  values indicate disequilibrium with the associated BMC antigorite serpentinites. For instance, carbonate values close to 9 ‰ are in equilibrium with serpentine (at 6.4 ‰) for temperatures around 300-400 °C, however the highest value (i.e. 16.64 ‰) would indicate equilibrium  $T < 100$  °C (Saccocia et al., 2009; Wenner and Taylor, 1971; Zheng, 1999, 1993) which is inconsistent with the antigorite-facies metamorphic evolution of the BMC (Guillot et al., 2015). From Figure 9, it can be observed that the variability of  $\delta^{13}\text{C}$  and  $\delta^{18}\text{O}$  of carbonate correlates with the distance from the graphite zone. This correlation is discussed in Section 5.2.

Raman spectroscopy of carbonaceous material (RSCM) present in metasedimentary sample V18-1a was conducted to estimate maximum temperature of graphite crystallization according to (Lünsdorf et al., 2014). Spectra collected ( $n=14$ ) indicate a temperature of  $435 \pm 14$  °C.

The  $\delta^{13}\text{C}$  and  $\delta^2\text{H}$  of  $\text{CH}_4$  extracted from fluid inclusions from the studied BMC and associated metasedimentary formations are available in Table 1. Fluid inclusions from metasedimentary sample V18-1 display a  $\delta^{13}\text{C}$  of -46.3 ‰ and  $\delta^2\text{H}$  of -226 ‰ for  $\text{CH}_4$  and a  $\delta^2\text{H}$  of -812 ‰ for  $\text{H}_2$  (Fig. 10A). Partially serpentinized peridotite (olivine-hosted) fluid inclusions from sample V18-2a show values of  $\delta^{13}\text{C}_{\text{CH}_4}$  of -12.6 ‰ and  $\delta^2\text{H}_{\text{CH}_4}$  of -171 ‰ while V18-11 show values of  $\delta^{13}\text{C}_{\text{CH}_4}$  of -45.2 ‰ and  $\delta^2\text{H}_{\text{CH}_4}$  of -226 ‰. Carbonate-hosted fluid inclusions from V18-4, V18-6d and V18-15 show values ranging from  $\delta^{13}\text{C}_{\text{CH}_4}$  of -15.5 ‰ and  $\delta^2\text{H}_{\text{CH}_4}$  of -168 ‰ to  $\delta^{13}\text{C}_{\text{CH}_4}$  of -31.3 ‰ and  $\delta^2\text{H}_{\text{CH}_4}$  of -177 ‰. Graphite-bearing titanite and plagioclase-hosted inclusions from

477 samples V18-12a,c and V18-14 shows values ranging from  $\delta^{13}\text{C}_{\text{CH}_4}$  of -12.6 ‰ and  
478  $\delta^2\text{H}_{\text{CH}_4}$  of -171 ‰ to  $\delta^{13}\text{C}_{\text{CH}_4}$  of -12.6 ‰ and  $\delta^2\text{H}_{\text{CH}_4}$  of -171 ‰.  $\text{H}_2$  was present in  
479 measurable amounts only in sample V18-12c and has a value  $\delta^2\text{H}_{\text{H}_2}$  of -680 ‰ (Fig.  
480 10B).

481  $\text{C}_1/\text{C}_2$  ratios are presented in Table 1 and show a low value of 13.23 for V18-1 typical  
482 of thermogenic sources (Martini et al., 2008), whereas samples from the BMC show a  
483 wider range of values. Olivine-hosted inclusions in sample V18-2a has a  $\text{C}_1/\text{C}_2$  ratio  
484 of 1992, while V18-11 have a value of 668. Carbonate-hosted fluid inclusions in V18-  
485 4 have a  $\text{C}_1/\text{C}_2$  ratio of 6154 and of 635 in V18-6d. The amount of  $\text{C}_2\text{H}_6$  is below the  
486 detection threshold in some samples leading to the absence of  $\text{C}_1/\text{C}_2$  ratio.

#### 487 4.6 Sr and B isotopes results

488 Strontium isotopic analyses were conducted on different BMC rock types and are  
489 presented in Table 1 and Figure 8B. The  $^{87}\text{Sr}/^{86}\text{Sr}$  of the sample V18-1a from the  
490 Ottawaquechee formation is 0.7578. The values of the BMC least serpentinized  
491 peridotites (V18-2a,b and V18-3a) range from 0.7082 to 0.7095 and  $^{87}\text{Sr}/^{86}\text{Sr}$  of least  
492 altered amphibolite (V18-14) is 0.7093. Serpentinite and samples from the graphite  
493 zones have similar  $^{87}\text{Sr}/^{86}\text{Sr}$  values between 0.7107 and 0.7177. Overall, the  $^{87}\text{Sr}/^{86}\text{Sr}$   
494 ratios of BMC samples is higher than Basaltic Achondrite Best Initial (BABI), and are  
495 not compatible with Mid-Ocean Ridge Basalt (MORB) signature and depleted mantle  
496 (DM) signature.

497 In a similar way, boron isotopes  $\delta^{11}\text{B}$  were investigated to assess fluid sources in the  
498 BMC.  $\delta^{11}\text{B}$  values are negative (Table 1, Fig. 8B). The  $\delta^{11}\text{B}$  of the Ottawaquechee  
499 formation (V18-1a) is -8.5 ‰. The  $\delta^{11}\text{B}$  of the BMC least serpentinized peridotites  
500 (V18-2a,b and V18-3a) ranges from -1.6 to -0.8 ‰ and  $\delta^{11}\text{B}$  of the least altered

amphibolite (18-14) is -3.49 ‰. Serpentinite samples (V18-7c and V18-10) and from graphite zone A (V18-5c) have  $\delta^{11}\text{B}$  values ranging from -4.6 to -2.4 ‰.

## 5 Discussion

### 5.1 Origin of the Belvidere graphite

The BMC graphite distribution and isotopic signatures suggest a fluid-deposited origin. The graphite concentrations in the BMC up to 3.91 wt% are very high compared to the average organic carbon content of subducted ultramafic and mafic rocks, usually clustering at 0.1 wt % (Alt and Teagle, 1999; Collins et al., 2015; Schwarzenbach et al., 2013; Shilobreeva et al., 2011). The graphite  $\delta^{13}\text{C}$  (-15.9 ‰,  $\pm 1\text{‰}$ ) in Zone A and (-15.3 ‰,  $\pm 1.2\text{‰}$ ) in zone B differs from the total organic carbon signature of subducted mafic and ultramafic rocks from -26.6 ‰ to -28 ‰ (Alt and Teagle, 1999; Collins et al., 2015; Schwarzenbach et al., 2013; Shilobreeva et al., 2011), and from mantle carbon at -10 ‰ to -4 ‰ (Deines, 1992; Javoy et al., 1986).

The graphite host rocks also confirm the hypothesis of fluid circulation and intense metasomatism. In particular, in graphite zone A, structural and geochemical features indicate that the rock was transiently enriched in Ca, Si and Al, as indicated by the presence of tremolite and chlorite, as observed in sample V18-Y1 with the formation of tremolite matrix sealing serpentine clasts (Fig. 5D). This stage is followed by graphite precipitation, as observed in samples V18-Yb and V18-5c, with the growth of tremolite crystals, the partial preservation of antigorite clasts and the precipitation of graphite coronae around tremolite crystals (Fig. 5(A,E)). Finally, the tremolite was statically replaced by antigorite, indicating a loss of Ca and enrichment in Mg, as observed in sample V18-5a (Fig. 5B). The collected samples suggest that this stage was more intense at the edges of graphite zone A. Carbonate precipitation at zone A

525 selvages may have occurred during the initial stages of fluid infiltration, or earlier.  
526 Microstructural features indicate that the initial stage of fluid infiltration was  
527 accompanied by fluid overpressure and brecciation, followed by intense syn-tremolite  
528 shear deformation, and finally static replacement of tremolite by antigorite.

529 In graphite zone B, graphite precipitated at the interface between ultramafic and mafic  
530 rocks. Also, in this case, petrography and microstructural analysis indicates that fluid  
531 overpressure was locally achieved in the mafic rocks adjacent to the ultramafic rocks,  
532 as indicated by brecciation of albite and precipitation of carbonate along fractures.  
533 These mineralogical and structural relationships indicate that the carbonate  
534 precipitation event took place at retrograde post-amphibolite greenschist-facies  
535 conditions (albite stable). The carbonate stable isotope signature may be consistent  
536 with an organic matter-rich metasedimentary fluid source (see also (Spandler et al.,  
537 2008) for similar interpretations in New Caledonia). This interpretation would be  
538 consistent with the regional setting of the BMC. The microstructural distribution of  
539 graphite, and the presence of CH<sub>4</sub>-rich fluid inclusions in the rock, may suggest a  
540 possible H<sub>2</sub>-mediated carbonate reduction as the origin of the graphite (Galvez et al.,  
541 2013; Giuntoli et al., 2020; Malvoisin et al., 2012; Peng et al., 2022; Vitale Brovarone  
542 et al., 2017). This is also suggested by some microstructures in graphite zone A (Fig.  
543 5E) and in other metamorphic settings in the presence of subduction zone  
544 serpentinization (Giuntoli et al., 2020; Vitale Brovarone et al., 2017). A prograde,  
545 closed system carbonate reduction (e.g., Tao et al., 2018) appears inconsistent with  
546 the retrograde timing of the graphite formation (syn-greenschist facies).



## 5.2 Source of carbon for methane formation

The graphite and methane isotopic composition alone does not allow identifying a clear carbon source. In particular, the graphite signature of  $\delta^{13}\text{C} = -17$  to  $-15$  ‰ may be compatible with either organic or inorganic sources, internal or external to the BMC. For example, graphite in metasedimentary rocks from Appalachian metasedimentary rocks shows  $\delta^{13}\text{C}$  ranging from about  $-27$  to  $-2$  ‰ (Evans et al., 2002; Zhang et al., 2018). Fluid-deposited graphite from New Hampshire, which is interpreted to derive from mixing of metasediment-derived fluids, shows  $\delta^{13}\text{C}$  values ranging from  $-29$  to  $-9$  ‰ (Rumble et al., 1986). The methane isotopic signature of  $\delta^{13}\text{C}$  and  $\delta^2\text{H}$  from BMC rocks indicates, at least in some samples, the contribution of biogenic organic matter (Fig. 10A). Samples V18-11, with an isotopic composition of  $-45.2$  ‰ for  $\delta^{13}\text{C}_{\text{CH}_4}$  and  $-226$  ‰ for  $\delta^2\text{H}_{\text{CH}_4}$  has values similar to the methane from graphite-rich metasedimentary sample V18-1 ( $-46.3$  ‰ for  $\delta^{13}\text{C}_{\text{CH}_4}$  and  $-226$  ‰ for  $\delta^2\text{H}_{\text{CH}_4}$ ). In other samples of partially serpentinized peridotite petrographically equivalent to V18-11, sample V18-2, the methane signature is very different ( $\delta^{13}\text{C}_{\text{CH}_4} -12.9$  ‰;  $\delta^2\text{H}_{\text{CH}_4} -171$  ‰), which may be consistent with processes involving various sources, including organic and inorganic (i.e., carbonate) sources, internal or external to the BMC.

The combination of  $^{87}\text{Sr}/^{86}\text{Sr}$  and  $\delta^{11}\text{B}$  data show a mixing trend between two end members (Fig. 8B), with a metasedimentary pole defined by V18-1 with low  $\delta^{11}\text{B}$  value ( $-8.48$  ‰) and extremely high  $^{87}\text{Sr}/^{86}\text{Sr}$  value (0.7578) and on the other end a serpentinized peridotite pole defined by V18-2b and V18-3a ( $\delta^{11}\text{B} = -0.83$  ‰ and  $-1.41$  ‰,  $^{87}\text{Sr}/^{86}\text{Sr} = 0.7095$  and  $0.7082$ ). The  $^{87}\text{Sr}/^{86}\text{Sr}$  values of the BMC ultramafic and mafic rocks are either higher relative to their protolith rocks, or seawater which suggest contamination by sedimentary or crustal reservoirs (Cannaò et al., 2016; Yamaoka et

571 al., 2012). The  $\delta^{11}\text{B}$  values of the BMC rocks are negative, which is consistent with  
572 serpentinization and metasomatism driven by the infiltration of metamorphic fluids  
573 (Martin et al., 2020), rather than seafloor metamorphism, which would result in much  
574 higher  $\delta^{11}\text{B}$ .

575 The presence of high nitrogen concentrations in the BMC fluid inclusions (enriched in  
576  $\text{N}_2$  and  $\text{NH}_3$  species) also suggests a metasedimentary source (Boutier et al., 2021  
577 and references therein). Additionally, the presence of abundant sulfur in the BMC fluid  
578 inclusions is also consistent with a metapelitic fluid source (Bebout and Fogel, 1992;  
579 Evans et al., 2014; Kelemen and Manning, 2015; Plank and Manning, 2019).

580 According to the above considerations, at least a part of the carbon in the system was  
581 sourced from the surrounding metasedimentary formations. However, the collected  
582 data also outline an internal production of  $\text{CH}_4$ . For example, SEM images suggests  
583 carbonates of the BMC as a potential source of carbon for methane production through  
584 reduction processes (Sections 4.2). The carbonate  $\delta^{13}\text{C}$  and  $\delta^{18}\text{O}$  data in the BMC  
585 ultramafic rocks may be interpreted as a reactional trend (Fig. 9). Graphite-free  
586 carbonated serpentinites (V18-6a and V18-14) show low carbonate  $\delta^{13}\text{C}$  and  $\delta^{18}\text{O}$   
587 values while carbonate from graphite-bearing ultramafic rocks (V18-7c and V18-5i)  
588 shows higher  $\delta^{13}\text{C}$  and  $\delta^{18}\text{O}$  values. Carbonate-graphite isotopic equilibrium would  
589 lead to unrealistic temperatures or gradients, from  $150^\circ\text{C}$  to  $550^\circ\text{C}$  from the graphite-  
590 free selvages to the center of graphite zone A based on fractionation factors from  
591 Bottinga, (1968). Instead, owing to the positive carbonate-methane isotopic  
592 fractionation during carbonate reduction, it is predicted to produce such a trend in the  
593 remaining carbonate fraction (Fig. 9; Galvez et al., 2013; Vitale Brovarone et al., 2017).  
594 Alternatively, because of the negative carbonate-carbon dioxide isotopic fractionation,

595 carbonate-silicate reactions producing carbon dioxide with increasing metamorphic  
596 conditions is known to induce a decrease in  $\delta^{13}\text{C}$  (Cook-Kollars et al., 2014; Piccoli et  
597 al., 2016; Valley, 1986) and could explain the reactional trend. However, the observed  
598 isotopic shift seems to correlate with the formation of graphite rather than with an  
599 increase in carbonate-silicate reactions. Based on the above considerations, the lower  
600  $\delta^{13}\text{C}$  carbonates are interpreted as the earliest ones in the studied BMC rocks. These  
601 values are low compared to marine carbonate and carbonate in ophiocarbonates  
602 (Collins et al., 2015). Such low initial values may have been achieved as a result of  
603 prograde decarbonation reactions, or from the precipitation of an isotopically light  
604 isotopic fluid source such as the above-mentioned graphite-bearing metasediment-  
605 derived fluid. A similar process was described for fluid-deposited carbonates found in  
606 metasomatized ultramafic rocks in New Caledonia (Spandler et al., 2008).

607 As outlined in Section 5.3, the evolution of the external metasediment-derived fluid  
608 during progressive serpentinization of the ultramafic body and its mixing with methane-  
609 rich reduced fluids resulting from carbonate reduction may easily overprint the original  
610  $\delta^{13}\text{C}$  of the infiltrating fluid in favor of the newly formed methane (i.e., the methane  
611 formed through carbonate reduction). Figure 10A shows the mixing trend between the  
612 metasedimentary source at  $\delta^{13}\text{C} = -45\text{‰}$   $\delta^2\text{H} = -240\text{‰}$  and the methane produced  
613 through carbonate reduction ranging from  $\delta^{13}\text{C} = -23\text{‰}$  to  $-12\text{‰}$  and  $\delta^2\text{H} = -140\text{‰}$ .  
614 Figure 11 shows that the model of methanation of carbonate from the BMC is  
615 consistent with the isotopic value of the methane ranging outside the thermogenic  
616 domain. However, such a trend could have been shifted to lower values by varying  
617 mixing trends with the isotopically lighter ( $\delta^{13}\text{C} = -45\text{‰}$ ) metasediment-derived fluid.

### 5.2.1 Fluid evolution and mechanism of graphite formation

Graphite precipitation may occur through multiple processes, which depend on the evolution of fluids and/or their interactions with the host rock. Four different mechanisms, which likely all together participated in the precipitation of graphite in the BMC, are considered in the present study, namely fluid dehydration –hereafter desiccation–, fluid mixing, changes in the ambient redox conditions, and carbonate reduction (Connolly, 1995; Duke and Rumble, 1986; Galvez et al., 2013; Holloway, 1984; Luque del Villar et al., 1998; Malvoisin et al., 2012; Vitale Brovarone et al., 2017). Other mechanisms, such as isobaric cooling or isothermal compression, are considered less plausible and will not be discussed further.

In a COH system, the graphite stability field is not only favored by with increasing pressure, and diminishes with increasing temperature (Cesare, 1995). Its stability is also dependent on the fluid component speciation, which is in turn dependent on the redox state of the system, and graphite can precipitate at fixed P-T conditions for varying fluid compositions and redox conditions. The redox state of a ternary COH system has been discussed as a function of the parameter  $X_O$  ( $X_O = \frac{n_O}{n_O + n_H}$ ) (Connolly, 1995; Connolly and Cesare, 1993). The maximum graphite stability for low carbon concentrations in a COH fluid is observed when the fluid-component speciation is dominantly  $H_2O$ , the so called “water maximum” ( $X_O = 1/3$ ). At fixed P and T, fluid infiltration can lead to graphite precipitation if  $X_O$  changes during the fluid-rock interaction. In a similar fashion, desiccation will lead to a change in the ratio of  $H_2O$ ,  $CO_2$ , and  $CH_4$  in the fluid and to the precipitation of graphite according to the following reaction:  $CH_4 + CO_2 = 2C + 2H_2O$  (Duke and Rumble, 1986). Fluid interactions have the potential to deposit graphite in amounts varying as a function of the intensity of the  $X_O$  variations. Desiccation leads to graphite precipitation proportional to the intensity

of the water loss. A micro-scale example of fluid desiccation is testified by the presence of olivine-hosted gaseous fluid inclusions filled with hydrous step-daughter minerals in the BMC, which indicate that the water present in the original entrapped fluids was progressively exhausted by hydration reactions of the inclusion walls (Boutier et al., 2021; see also Klein et al., 2019). With progressive exhaustion of the H<sub>2</sub>O component and residual enrichment of carbon in the remaining fluid, the system may reach carbon saturation and graphite precipitation (see also Andreani et al. (2023) for the precipitation of different carbonaceous complexes). Graphite was found only locally as a step-daughter mineral in the BMC fluid inclusions (Boutier et al., 2021). This indicates that fluid desiccation inside the fluid inclusions cannot account for the precipitation of substantial graphite amounts along shear zones and lithologic boundaries as observed in the BMC. However, the desiccation process may have taken place at larger scales during the progressive infiltration of metamorphic fluids responsible for the partial hydration of the BMC ultramafic rocks.

Based on the collected data, the main fluid infiltration event can be described as an H<sub>2</sub>O-rich fluid equilibrated with a carbon-bearing metasedimentary source. Sample V18-1 suggests that this fluid may have had a low  $\delta^{13}\text{C}$  signature (Table 1). This initial isotopic composition may be preserved in the fluid inclusions of samples V18-11 and V18-14, as indicated by the  $\delta^{13}\text{C}$  and  $\delta^2\text{H}$  values of CH<sub>4</sub>. A slightly reduced ( $X_{\text{O}} \lesssim \frac{1}{3}$ ) graphite-saturated COH fluid near water maximum can be dominated by CH<sub>4</sub> with respect to CO<sub>2</sub>. For instance, a carbon-saturated COH fluid at  $X_{\text{O}}=0.33$  (QFM -0.5) at 450 °C and 1.1 GPa (conditions estimated for the hydration of the peridotite body and consistent with the thermal metamorphic peak of the surrounding metasedimentary units, Boutier et al., 2021) would consist of 98% (molar) of H<sub>2</sub>O with a  $\frac{CO_2}{CH_4+CO_2}=0.32$ . Such fluid would have plenty of water available to hydrate the peridotite body. This

hypothesis is supported by the fluid inclusion composition (Boutier et al., 2021) and bulk-rock isotopic signatures discussed in the previous sections, which all together suggest serpentinization by metasediment-derived fluids. Owing to the formation of hydrous phases such as antigorite and chlorite and to the partial oxidation of iron to form magnetite, the evolution of this externally derived fluid during serpentinization would encounter two important changes, which are progressive desiccation and reduction. The decreasing  $fO_2$  during metamorphic serpentinization of the BMC may have in fact enhanced the conversion of the more oxidized fraction (e.g., carbon dioxide, bicarbonates) of the infiltrating fluid to additional methane. Because a carbon-saturated fluid at water maximum corresponds to the minimum of carbon solubility, desiccation of this fluid toward more reducing conditions would increase the fraction of carbon in the fluid in favor of methane-dominated compositions. This process, described by the model in Figure 12A-D, may precipitate graphite. The model considers desiccation of 100 moles of metasediment-derived fluid at 450 °C and 1.1 GPa in a closed system. The initial redox state of the fluid was set slightly below the water maximum ( $X_{O_2} = 0.33$ ) in order to allow the model to spontaneously proceed toward more reducing conditions during desiccation (Fig. 12A-C). The model predicts that full desiccation of this fluid would precipitate 1.24 moles of graphite (per 100 moles of initial fluid, Fig. 12D). However, this model fails at reproducing the graphite isotopic compositions as measured in the BMC sample. Considering an infiltrating fluid with  $\delta^{13}C = -45\text{‰}$  (as measured in samples V18-1A and V18-11), desiccation would lead to the precipitation of graphite with a too low  $\delta^{13}C$  signature (Fig. 12E). A plausible way to obtain relative heavier  $\delta^{13}C$  value is the participation of carbonate present in the BMC mafic and ultramafic rocks. The BMC rocks present evidence of carbonate reduction, as illustrated by SEM imaging (V18-7c) (Fig. 5D), suggesting reduction of

dolomite into calcite and brucite along with the release of CH<sub>4</sub> and H<sub>2</sub>O (Peng et al., 2021), and formation of graphite around dolomite relicts. The reduction of carbonate in the ultramafic body, favored by decreasing  $fO_2$  in the evolved infiltrating fluid, could additionally increase the methane concentration in the fluid and impose a heavier isotopic composition to the fluid. Isotopically labeled dissolution experiments of carbonate-graphite mixtures have shown that the isotopic composition of graphite-derived CO<sub>2</sub> can be buffered by the isotopic composition of carbonate, regardless of the carbonate/graphite ratios (Tumiati et al., 2022). Those experiments did not consider reducing conditions. However, considering that the reduction of carbonate releases more carbon than carbonate dissolution in pure water (Lazar et al., 2012), and that the initial infiltrating fluid likely was water-rich and carbon-poor (near the water maximum), it can be expected that the carbon isotopic composition of the precipitated graphite was controlled more by the carbonate than the desiccated infiltrating fluid. Moreover, the infiltrating fluid was initially water-dominated, and its desiccation would produce a much smaller amounts of carbon-rich fluid, favoring carbonate as a carbon isotopic buffer. In this case, the transformation of methane at  $\delta^{13}C = -23\text{‰}$  produced from the reduction of the least altered carbonate in the BMC ultramafic rocks would lead to the precipitation of graphite with  $\delta^{13}C = -15\text{‰}$  to  $-16.5\text{‰}$  at 400-450°C. This calculated  $\delta^{13}C$  range fits well the range of  $\delta^{13}C$  values measured for the BMC graphite and could explain its precipitation mechanism through coupled desiccation and carbonate reduction. Furthermore, the participation of carbonate in the graphite precipitation mechanism may explain the mineralogical variations within graphite zone A, with replacement of antigorite by tremolite.

The distribution of graphite in the BMC along shear zones and lithologic boundaries suggests that these structures acted as major fluid channels. Although the mechanism

of graphite precipitation presented above may explain the measured graphite  $\delta^{13}\text{C}$  values, it represents a static, or instantaneous process, with one single fluid influx from the surrounding metasedimentary rocks. Because a more realistic, dynamic process may imply continuous or multiple fluid influx from the surrounding metasedimentary units and the migration of the evolved fluids outside the BMC, we also consider a graphite precipitation model involving mixing between the metasediment-derived fluid and its evolved (desiccation + carbonate reduction) equivalent.

In this model, presented in Figure 12F-J, the mixing of an external metasedimentary fluid with a  $\delta^{13}\text{C}$  of methane at -45‰ (sample V18-1) and a methane-rich fluid around  $\delta^{13}\text{C} = -23\text{‰}$  (samples V18-2 and V18-4) formed inside the BMC, would lead to the precipitation of graphite at  $\delta^{13}\text{C} = -14\text{‰}$  to -18 ‰ at 450°C and 1.1 GPa (pressure constrained by Honsberger, 2015; Laird et al., 1993 for the BMC) (Fig. 12J). The amount of graphite precipitated through this mechanism is estimated to be 1.39 mol for 200 mol of fluid and corresponds to 5% of the carbon in the initial fluid (Fig. 12).

This model shows that the observed carbon isotope values of graphite, carbonate, and methane can be explained through the infiltration of a single low  $\delta^{13}\text{C}$  fluid, its evolution during serpentinization inside the BMC, and their remixing along major fluid channels. The escape of the strongly reduced fluid formed in response to serpentinization may have encountered redox variations while reaching the surrounding rocks. This may also participate in the formation of graphite-rich rocks in graphite zone B. The BMC would act as an open system with infiltration localized along fluid channels with initial intake of metasedimentary equilibrated water and outtake of serpentinization-related reduced fluid.



741 The above models are also supported the silicate fraction of the graphite-rich rocks.  
742 Samples from graphite zone A show an initial Ca enrichment and Sr isotopic signature  
743 consistent with metasediment-derived fluids, followed by a Ca depletion and Mg  
744 enrichment, which may be consistent with a reinjection of evolved, serpentinization-  
745 related fluids inside a preferential fluid pathway such as graphite zones A and B. The  
746 petrological features observed at the edge of the graphite zone A are consistent with  
747 the escape of an internal Mg-rich fluid leading to the retromorphism of tremolite  
748 crystals to antigorite (V18-5a)(Fig. 5B).

749 In summary, the precipitation of graphite in the BMC can be summarized in four majors  
750 steps, as follows, and is illustrated in an idealized sketch in Figure 13:

751 1- The BMC was infiltrated by metasediment-derived fluids, resulting in metasomatism  
752 (e.g, Ca enrichment; negative  $\delta^{11}\text{B}$ ; high  $^{87}\text{Sr}/^{86}\text{Sr}$ ) along major fluid channels (e.g.  
753 graphite zones A and B).

754 2- This fluid progressively equilibrated with the BMC ultramafic rocks during pervasive  
755 serpentinization in the antigorite stability field and may be responsible for the  
756 precipitation of isotopically light carbonate in the BMC rocks.

757 3- The metamorphic serpentinization of the BMC led to progressive desiccation of the  
758 infiltrating fluid and decreasing  $f\text{O}_2$  conditions, which promoted additional methane  
759 formation through carbonate reduction and/or respeciation of more oxidized fluids.  
760 These processes may have participated in the precipitation of graphite.

761 4- The  $\text{CH}_4$ -enriched fluids resulting from the BMC serpentinization and carbonate  
762 reduction were reinjected along fluid channels, causing additional metasomatism (Mg

enrichment and Ca depletion) and favoring fluid mixing and additional graphite precipitation.

### 5.3 Consideration on the origin of metamorphic methane in the BMC

The BMC methane is an example of an increasing number of reports of methane in subduction zone metamorphic rocks. Abiotic methanogenesis in ultramafic rocks has been shown at natural conditions spanning seafloor hydrothermalism, magmatism, and on-land surficial serpentinization (e.g., Etiope and Sherwood Lollar, 2013). This is an important process in deep subsurface biosphere research and geoastronomy, as it is considered as a source of prebiotic organic compounds and their possible role on the origin of life on Earth and potentially elsewhere (Colman et al., 2017; Holm et al., 2015; Schulte et al., 2006).

The initial infiltrating fluid of the proposed evolution may have contained CH<sub>4</sub>. If this fluid equilibrates at water maximum, graphite-saturated conditions, a roughly comparable concentration of CH<sub>4</sub> and CO<sub>2</sub> is expected. Sample V18-1 from the Ottawuechee metasedimentary formation contains CH<sub>4</sub> in fluid inclusions. This CH<sub>4</sub> can be interpreted as methane formed as a result of graphite-saturated COH thermodynamics, as conventionally proposed for metapelitic rocks, which would be by definition abiotic. However, the analyzed  $\delta^{13}\text{C}$  and  $\delta^2\text{H}$  data of CH<sub>4</sub> from this sample indicate a thermogenic origin, which is classically considered as biotic. Thermogenic production of CH<sub>4</sub> is generally believed to be limited to about 300 °C (Mangenot et al., 2018; Stolper et al., 2015, 2014). The Ottawuechee metasediments experienced metamorphism to about 434 °C, as indicated by RSCM thermometry. This temperature

786 is well above the conventional limit of thermogenic methane. The interaction of this  
787 fluid with the BMC promoted serpentinization and additional reduction of the fluid.  
788 During this event, the CO<sub>2</sub> present in the infiltrating fluid (for reference, a graphite  
789 saturated fluid at 400 °C, 1.0 GPa, and X<sub>o</sub> = 0.333 contains a CH<sub>4</sub>/CO<sub>2</sub> ratio of 1) is  
790 expected to be converted into CH<sub>4</sub> through a process of CO<sub>2</sub> reduction that is, by  
791 definition, abiotic. However, its signature would still appear biotic.

792 The reduction of carbonates by the serpentinization-related reducing fluids promoted  
793 additional formation of methane. This methane must be considered abiotic in origin  
794 and, depending on the degree of mixing with the external fluid, may still record its  
795 inorganic source. However, in the case of the BMC, the isotopic signature of the  
796 reactant carbonates was negative (-7.26 to -1.43 ‰) and was potentially affected by  
797 previous interaction with fluids recording an organic carbon source.

798 Grozeva et al., 2020 report δ<sup>13</sup>C isotopic values for abiotic methane in inclusions from  
799 two active serpentinization systems ranging from -16.7 ‰ to -4.4 ‰ in the Von Damm  
800 hydrothermal field and ranging from -12.4 ‰ to -2.8 ‰ for the Zambales ophiolite. In  
801 both datasets C1/C2 values range from 163 to 1372 and cluster around 400. The main  
802 mechanism proposed for methane formation is the conversion of mantle CO<sub>2</sub> to CH<sub>4</sub>  
803 and the carbon isotopic composition of the CH<sub>4</sub> reflects the isotopic composition of  
804 mantle CO<sub>2</sub> along with variations caused by the carbon isotopic composition in the  
805 host rock. Data from Grozeva et al. 2020 are akin to values of V18-2 and V18-4 fluid  
806 inclusions reflecting the abiotic hydrocarbon production of the BMC. However, the fluid  
807 composition of the BMC (rich in C, N, and S) strongly differs from the inclusions  
808 analyzed by Grozeva et al. 2020, and the collected data point to a different,  
809 metamorphic origin in the Taconic subduction zone.

The distribution of more biotic or abiotic signatures across the BMC depict the complexity of the process of fluid infiltration and fluid-rock interactions that affected the massif. Also, the collected data stress the complexity of methane generation and evolution in metamorphic settings and call for additional analyses on these metamorphic gases. In particular methane clumped isotope analysis has proven to provide additional insight on the discrimination between biotic and abiotic processes (Ono et al., 2021; Shuai et al., 2018; Young et al., 2017).

In conclusion, the results obtained in this work indicate that the origin and chemistry of metamorphic methane can be more complex than previously assumed.

#### 5.4 Implication on large scale methane production

Subducted fresh ultramafic bodies can act as massive converter factories of CO<sub>2</sub> into CH<sub>4</sub> and other reduced carbon phases such as graphite. Because these fluids circulate in the subduction channel, they can have a significant impact on the redox budgets in the subduction zone. Redox barriers, that is an interface between two compartments with a steep difference in redox conditions, imposed at lithological contacts for example, can act as carbon sinks, such as graphite deposition, effectively halting a percentage of the C transfer in metamorphic fluids.

When considering next the serpentizing mantle wedge, which could similarly act as a powerhouse of H<sub>2</sub> and CH<sub>4</sub> formation, the path taken by the resultant fluids will impact significantly on the formation or precipitation of these compounds. This can in turn hamper the quantification of the methane release from subduction zones, as many redox barriers – including the activity of microorganisms within the biosphere – can be expected within the mantle wedge and above inside the crust.

## 6 Conclusions

834 Petrological, Raman, and isotopic data provided additional insights on the fate of  
835 carbon at the Belvidere Mountain Complex, Appalachian belt, Northern Vermont. The  
836 exceptional graphite deposit observed across the study site highlights limitations on  
837 carbon mobility in the subduction zone and the complex mechanism of fluid interaction  
838 with evolving redox conditions. The carbon, strontium, and boron isotopes indicate  
839 fluid infiltrations evolving from metasedimentary rocks in subduction zones as the  
840 initial fluid influx responsible for the high-pressure serpentinization and the first  
841 metasomatic event. This is consistent with the model proposed by Kerper et al. (2008).  
842 Isotopic investigation of methane in fluid inclusions highlights a complex evolution  
843 involving both metasediment-derived, high-temperature thermogenic (biotic) and  
844 serpentinization-related (abiotic) CH<sub>4</sub>-forming processes. Collected data and  
845 numerical results point toward graphite precipitation as the results of the mixing of CH<sub>4</sub>  
846 released by the HP serpentinization of the BMC with more oxidized infiltrating fluid  
847 (possibly the same fluid driving the serpentinization). This study outlines that ultramafic  
848 bodies in subduction can retain their potential to be abiotic producers of methane  
849 during relatively shallow subduction conditions (before antigorite destabilization).  
850 However, the redox state of surrounding formations seems to play an important role  
851 as it could severely impede fluid mobility of carbon. In this scope, the mantle wedge  
852 interacting with the slab as a source of water and carbon could host similar reactions,  
853 with implications for the redox state of subduction, carbon cycling in subduction and  
854 for the interpretation of biotic vs. abiotic signatures on earth and potentially beyond. A  
855 recent study highlights such a phenomenon with the high oxidation potential of the  
856 metasedimentary cover of the slab demonstrating capability to convert a high amount  
857 of fluid (Ague et al., 2022).

## 858 7 Acknowledgment

859 The authors wish to thank Leslie White for fundamental support during the field work.  
860 IFP Energies Nouvelles and its helpful personnel is thanked for their help in the  
861 acquisition on test isotopic data of methane. This work is part of a project that has  
862 received funding from the European Research Council (ERC) under the European  
863 Union's Horizon 2020 research and innovation program (Grant agreement No.  
864 864045; project acronym DeepSeep). A MIUR Rita Levi Montalcini grant and a Richard  
865 Lounsbery grant to AVB are also acknowledged. Andrea Risplendente is thanked for  
866 assistance during microprobe analysis.

867

## 8 Appendix A. Supplementary materials

Supplementary material 1 is a table providing uncertainties and detection limits for whole-rock analyses.

Supplementary material 2 includes microRaman spectroscopy results of fluids inclusions in calcite, quartz, olivine, plagioclase, and titanite. The presence of CH<sub>4</sub>, H<sub>2</sub>, N<sub>2</sub>, and H<sub>2</sub>S is shown.

Supplementary material 3 contains bulk-rock major and REE compositions of the studied rock samples. The patterns suggest that graphite zones A and B formed at the expense of ultramafic rocks.

Supplementary material 4 presents the complete carbon, oxygen, and hydrogen isotopic data from solid and fluid phases and the related uncertainties from different acquisition methods (Picarro and GC-MS).

## 9 References

- Agostini, S., Di Giuseppe, P., Manetti, P., Doglioni, C., Conticelli, S., 2021. A heterogeneous subcontinental mantle under the African–Arabian Plate boundary revealed by boron and radiogenic isotopes. *Sci. Rep.* 11, 11230.
- Agostini, S., Di Giuseppe, P., Manetti, P., Savaşçın, M.Y., Conticelli, S., 2022. Geochemical and isotopic (Sr-Nd-Pb) signature of crustal contamination in Na-alkali basaltic magmas of South-East Turkey. *Ital. J. Geosci.* 141, 363–384.
- Ague, J.J., 2017. Element mobility during regional metamorphism in crustal and subduction zone environments with a focus on the rare earth elements (REE). *Am. Mineral.* 102, 1796–1821.
- Ague, J.J., Nicolescu, S., 2014. Carbon dioxide released from subduction zones by fluid-mediated reactions. *Nat. Geosci.* 7, 355.
- Ague, J.J., Tassara, S., Holycross, M.E., Li, J.-L., Cottrell, E., Schwarzenbach, E.M., Fassoulas, C., John, T., 2022. Slab-derived devolatilization fluids oxidized by subducted metasedimentary rocks. *Nat. Geosci.* 1–7.
- Alt, J.C., Teagle, D.A., 1999. The uptake of carbon during alteration of ocean crust. *Geochim. Cosmochim. Acta* 63, 1527–1535.
- Andreani, M., Montagnac, G., Fellah, C., Hao, J., Vandier, F., Daniel, I., Pisapia, C., Galipaud, J., Lilley, M.D., Fröh Green, G.L., 2023. The rocky road to organics needs drying. *Nat. Commun.* 14, 347.

- Bebout, G.E., 1991. Field-based evidence for devolatilization in subduction zones: implications for arc magmatism. *Science* 251, 413–416.
- Bebout, G.E., Barton, M.D., 1993. Metasomatism during subduction: products and possible paths in the Catalina Schist, California. *Chem. Geol.* 108, 61–92.
- Bebout, G.E., Fogel, M.L., 1992. Nitrogen-isotope compositions of metasedimentary rocks in the Catalina Schist, California: implications for metamorphic devolatilization history. *Geochim. Cosmochim. Acta* 56, 2839–2849.
- Bottinga, Y., 1969. Calculated fractionation factors for carbon and hydrogen isotope exchange in the system calcite-carbon dioxide-graphite-methane-hydrogen-water vapor. *Geochim. Cosmochim. Acta* 33, 49–64.
- Bottinga, Y., 1968. Isotopic fractionation in the system: calcite–graphite–carbon dioxide–methane–hydrogen–water. N P 1968 Web.
- Boutier, A., Vitale Brovarone, A., Martinez, I., Sissmann, O., Mana, S., 2021. High-pressure serpentinization and abiotic methane formation in metaperidotite from the Appalachian subduction, northern Vermont. *Lithos* 106190.
- Bradley, A.S., Summons, R.E., 2010. Multiple origins of methane at the Lost City Hydrothermal Field. *Earth Planet. Sci. Lett.* 297, 34–41.
- Breitenbach, S.F., Bernasconi, S.M., 2011. Carbon and oxygen isotope analysis of small carbonate samples (20 to 100 µg) with a GasBench II preparation device. *Rapid Commun. Mass Spectrom.* 25, 1910–1914.
- Cannaò, E., Scambelluri, M., Agostini, S., Tonarini, S., Godard, M., 2016. Linking serpentinite geochemistry with tectonic evolution at the subduction plate-interface: The Voltri Massif case study (Ligurian Western Alps, Italy). *Geochim. Cosmochim. Acta* 190, 115–133.
- Carlsen, K.S., Gale, M.H., Thompson, W.B., Kierstead, M., 2015. Belvidere Mountain Asbestos Quarries, Lowell/Eden, Vermont. *Rocks Miner.* 90, 510–551.
- Castonguay, S., Kim, J., Thompson, P.J., Gale, M.H., Joyce, N., Laird, J., Doolan, B.L., 2012. Timing of tectonometamorphism across the Green Mountain anticlinorium, northern Vermont Appalachians:  $^{40}\text{Ar}/^{39}\text{Ar}$  data and correlations with southern Quebec. *GSA Bull.* 124, 352–367.
- Cesare, B., 1995. Graphite precipitation in C–O–H fluid inclusions: closed system compositional and density changes, and thermobarometric implications. *Contrib. Mineral. Petrol.* 122, 25–33.
- Chew, D.M., van Staal, C.R., 2014. The ocean–continent transition zones along the Appalachian–Caledonian Margin of Laurentia: Examples of large-scale hyperextension during the opening of the Iapetus Ocean. *Geosci. Can.* 41, 165–185.
- Chidester, A.H., Albee, A.L., Cady, W.M., 1978. Petrology, structure, and genesis of the asbestos-bearing ultramafic rocks of the Belvidere Mountain area in Vermont. US Govt. Print. Off.,.
- Clift, P.D., 2017. A revised budget for Cenozoic sedimentary carbon subduction. *Rev. Geophys.* 55, 97–125.
- Collins, N.C., Bebout, G.E., Angiboust, S., Agard, P., Scambelluri, M., Crispini, L., John, T., 2015. Subduction zone metamorphic pathway for deep carbon cycling: II. Evidence from HP/UHP metabasaltic rocks and ophicarbonates. *Chem. Geol.* 412, 132–150.
- Colman, D.R., Poudel, S., Stamps, B.W., Boyd, E.S., Spear, J.R., 2017. The deep, hot biosphere: Twenty-five years of retrospection. *Proc. Natl. Acad. Sci.* 114, 6895–6903.
- Connolly, J.A.D., 1995. Phase diagram methods for graphitic rocks and application to the system C–O–H–FeO–TiO<sub>2</sub>–SiO<sub>2</sub>. *Contrib. Mineral. Petrol.* 119, 94–116.
- Connolly, J.A.D., Cesare, B., 1993. C–O–H–S fluid composition and oxygen fugacity in graphitic metapelites. *J. Metamorph. Geol.* 11, 379–388.



951 Cook-Kollars, J., Bebout, G.E., Collins, N.C., Angiboust, S., Agard, P., 2014. Subduction zone  
 952 metamorphic pathway for deep carbon cycling: I. Evidence from HP/UHP  
 953 metasedimentary rocks, Italian Alps. *Chem. Geol.* 386, 31–48.  
 954 Dasgupta, R., 2013. Ingassing, Storage, and Outgassing of Terrestrial Carbon through Geologic  
 955 Time. *Rev. Mineral. Geochem.* 75, 183–229.  
 956 Dasgupta, R., Hirschmann, M.M., 2010. The deep carbon cycle and melting in Earth's interior.  
 957 *Earth Planet. Sci. Lett.* 298, 1–13.  
 958 Debret, B., Bolfan-Casanova, N., Padrón-Navarta, J.A., Martin-Hernandez, F., Andreani, M.,  
 959 Garrido, C.J., Sanchez-Vizcaino, V.L., Gómez-Pugnaire, M.T., Munoz, M., Trcera, N.,  
 960 2015. Redox state of iron during high-pressure serpentinite dehydration. *Contrib.*  
 961 *Mineral. Petrol.* 169, 36.  
 962 Deines, P., 1992. Mantle carbon: concentration, mode of occurrence, and isotopic composition,  
 963 in: *Early Organic Evolution*. Springer, pp. 133–146.  
 964 Deschamps, F., Godard, M., Guillot, S., Hattori, K., 2013. Geochemistry of subduction zone  
 965 serpentinites: A review. *Lithos* 178, 96–127.  
 966 Duke, E.F., Rumble, D., 1986. Textural and isotopic variations in graphite from plutonic rocks,  
 967 south-central New Hampshire. *Contrib. Mineral. Petrol.* 93, 409–419.  
 968 Etiope, G., Sherwood Lollar, B., 2013. Abiotic methane on Earth. *Rev. Geophys.* 51, 276–299.  
 969 Evans, K.A., 2012. The redox budget of subduction zones. *Earth-Sci. Rev.* 113, 11–32.  
 970 Evans, K.A., Bickle, M.J., Skelton, A.D.L., Hall, M., Chapman, H., 2002. Reductive deposition  
 971 of graphite at lithological margins in East Central Vermont: a Sr, C and O isotope study.  
 972 *J. Metamorph. Geol.* 20, 781–798.  
 973 Evans, K.A., Tomkins, A.G., Cliff, J., Fiorentini, M.L., 2014. Insights into subduction zone  
 974 sulfur recycling from isotopic analysis of eclogite-hosted sulfides. *Chem. Geol.* 365, 1–  
 975 19.  
 976 Facq, S., Daniel, I., Montagnac, G., Cardon, H., Sverjensky, D.A., 2014. In situ Raman study  
 977 and thermodynamic model of aqueous carbonate speciation in equilibrium with  
 978 aragonite under subduction zone conditions. *Geochim. Cosmochim. Acta* 132, 375–  
 979 390.  
 980 Foster, G.L., 2008. Seawater pH, pCO<sub>2</sub> and [CO<sub>2</sub><sup>-3</sup>] variations in the Caribbean Sea over the  
 981 last 130 kyr: A boron isotope and B/Ca study of planktic foraminifera. *Earth Planet.*  
 982 *Sci. Lett.* 271, 254–266.  
 983 Frezzotti, M.L., Selverstone, J., Sharp, Z.D., Compagnoni, R., 2011. Carbonate dissolution  
 984 during subduction revealed by diamond-bearing rocks from the Alps. *Nat. Geosci.* 4,  
 985 703–706.  
 986 Frezzotti, M.L., Tecce, F., Casagli, A., 2012. Raman spectroscopy for fluid inclusion analysis.  
 987 *J. Geochem. Explor.* 112, 1–20.  
 988 Fumagalli, P., Klemme, S., 2015. Phase transitions and mineralogy of the upper mantle.  
 989 *Treatise on Geophysics*. 2, Mineral Physics, 7-31.  
 990 Gale, M.H., 1980. Geology of the Belvidere Mountain Complex, Eden and Lowell, Vermont.  
 991 US Geological Survey.  
 992 Galvez, M.E., Beyssac, O., Martinez, I., Benzerara, K., Chaduteau, C., Malvoisin, B.,  
 993 Malavieille, J., 2013. Graphite formation by carbonate reduction during subduction.  
 994 *Nat. Geosci.* 6, 473.  
 995 Giovannelli, D., Barry, P.H., de Moor, J.M., Jessen, G.L., Schrenk, M.O., Lloyd, K.G., 2022.  
 996 Sampling across large-scale geological gradients to study geosphere–biosphere  
 997 interactions. *Front. Microbiol.* 13, 998133.  
 998 Giuntoli, F., Vitale Brovarone, A., Menegon, L., 2020. Feedback between high-pressure  
 999 genesis of abiotic methane and strain localization in subducted carbonate rocks. *Sci.*  
 1000 *Rep.* 10, 1–15.

1001 Gold, T., 1992. The deep, hot biosphere. *Proc. Natl. Acad. Sci.* 89, 6045–6049.

1002 Gorman, P.J., Kerrick, D.M., Connolly, J. a. D., 2006. Modeling open system metamorphic  
1003 decarbonation of subducting slabs. *Geochem. Geophys. Geosystems* 7.  
1004 <https://doi.org/10.1029/2005GC001125>

1005 Green, D.H., Falloon, T.J., Taylor, W.R., 1987. Mantle-derived magmas-roles of variable  
1006 source peridotite and variable CHO fluid compositions. *Magmat. Process.*  
1007 *Physicochem. Princ.* 1, 139–154.

1008 Grozeva, N.G., Klein, F., Seewald, J.S., Sylva, S.P., 2020. Chemical and isotopic analyses of  
1009 hydrocarbon-bearing fluid inclusions in olivine-rich rocks. *Philos. Trans. R. Soc. A*  
1010 378, 20180431.

1011 Guillot, S., Schwartz, S., Reynard, B., Agard, P., Prigent, C., 2015. Tectonic significance of  
1012 serpentinites. *Tectonophysics* 646, 1–19.

1013 Hayes, J.M., Waldbauer, J.R., 2006. The carbon cycle and associated redox processes through  
1014 time. *Philos. Trans. R. Soc. Lond. B Biol. Sci.* 361, 931–950.

1015 Holloway, J.R., 1984. Graphite-CH<sub>4</sub>-H<sub>2</sub>O-CO<sub>2</sub> equilibria at low-grade metamorphic  
1016 conditions. *Geology* 12, 455–458.

1017 Holm, N.G., Oze, C., Mousis, O., Waite, J.H., Guilbert-Lepoutre, A., 2015. Serpentinization  
1018 and the Formation of H<sub>2</sub> and CH<sub>4</sub> on Celestial Bodies (Planets, Moons, Comets).  
1019 *Astrobiology* 15, 587.

1020 Honsberger, I.W., 2023. Newly recognized blueschist-facies metamorphism (glaucophane-  
1021 omphacite-garnet), Belvidere Mountain Complex, northern Appalachians. *Geosphere*.  
1022 <https://doi.org/10.1130/GES02582.1>

1023 Honsberger, I.W., 2015. Metamorphism, deformation, geochemistry, and tectonics of exhumed  
1024 ultramafic and mafic rocks in the central and north-central Vermont Appalachians. PhD  
1025 Diss Univ. N. H.

1026 Honsberger, I.W., Laird, J., Thompson, P.J., 2017. A tectonized ultramafic-mafic-pelitic  
1027 package in Stockbridge, Vermont: Metamorphism resulting from subduction and  
1028 exhumation. *Am. J. Sci.* 317, 1019–1047.

1029 Huizenga, J.M., 2005. COH, an Excel spreadsheet for composition calculations in the COH  
1030 fluid system. *Comput. Geosci.* 31, 797800.

1031 Javoy, M., Pineau, F., Delorme, H., 1986. Carbon and nitrogen isotopes in the mantle. *Chem.*  
1032 *Geol.* 57, 41–62.

1033 Kelemen, P.B., Manning, C.E., 2015. Reevaluating carbon fluxes in subduction zones, what  
1034 goes down, mostly comes up. *Proc. Natl. Acad. Sci.* 112, E3997–E4006.

1035 Kerper, D., van Baalen, M.R., Dunn, S., 2008. Anomalous graphite at the Belvidere Mountain  
1036 serpentinite, Vermont, in: *GSA Northeastern Regional Meeting*, Buffalo, New York.  
1037 pp. 12–35.

1038 Kerrick, D.M., Connolly, J. a. D., 1998. Subduction of ophiicarbonates and recycling of CO<sub>2</sub>  
1039 and H<sub>2</sub>O. *Geology* 26, 375–378.

1040 Kerrick, D.M., Connolly, J.A.D., 2001a. Metamorphic devolatilization of subducted marine  
1041 sediments and the transport of volatiles into the Earth's mantle. *Nature* 411, 293–296.

1042 Kerrick, D.M., Connolly, J.A.D., 2001b. Metamorphic devolatilization of subducted oceanic  
1043 metabasalts: implications for seismicity, arc magmatism and volatile recycling. *Earth*  
1044 *Planet. Sci. Lett.* 189, 19–29.

1045 Klein, F., Grozeva, N.G., Seewald, J.S., 2019. Abiotic methane synthesis and serpentinization  
1046 in olivine-hosted fluid inclusions. *Proc. Natl. Acad. Sci.* 116, 17666–17672.

1047 Labotka, T.C., Albee, A.L., 1979. Serpentinization of the Belvidere Mountain ultramafic body,  
1048 Vermont; mass balance and reaction at the metasomatic front. *Can. Mineral.* 17, 831–  
1049 845.

- 1050 Laird, J., Bothner, W.A., Thompson, P.J., Thompson, T., Gale, M., Kim, J., 2001.  
1051 Geochemistry, petrology, and structure of the Tillotson Peak and Belvidere Mountain  
1052 mafic complexes, northern Vermont, in: Geological Society of America Abstracts with  
1053 Programs. p. A59.
- 1054 Laird, J., Trzcieski, W.E., Bothner, W.A., Cheney, J.T., Hepburn, J.C., 1993. High-pressure,  
1055 Taconian, and subsequent polymetamorphism of southern Quebec and northern  
1056 Vermont. *Contrib. Dep. Univ. Mass.* 67, 1–32.
- 1057 Lazar, C., McCollom, T.M., Manning, C.E., 2012. Abiogenic methanogenesis during  
1058 experimental komatiite serpentinization: implications for the evolution of the early  
1059 Precambrian atmosphere. *Chem. Geol.* 326, 102–112.
- 1060 Lünsdorf, N.K., Dunkl, I., Schmidt, B.C., Rantitsch, G., von Eynatten, H., 2014. Towards a  
1061 higher comparability of geothermometric data obtained by Raman spectroscopy of  
1062 carbonaceous material. Part I: Evaluation of biasing factors. *Geostand. Geoanalytical*  
1063 *Res.* 38, 73–94.
- 1064 Luque del Villar, F.J., Pasteris, J.D., Wopenka, B., Rodas, M., Fernández Barrenechea, J.M.,  
1065 1998. Natural fluid-deposited graphite: mineralogical characteristics and mechanisms  
1066 of formation. *Am. J. Sci.* 298, 471–498.
- 1067 Malvoisin, B., Chopin, C., Brunet, F., Galvez, M.E., 2012. Low-temperature wollastonite  
1068 formed by carbonate reduction: a marker of serpentinite redox conditions. *J. Petrol.* 53,  
1069 159–176.
- 1070 Mangenot, X., Gasparrini, M., Rouchon, V., Bonifacie, M., 2018. Basin-scale thermal and fluid  
1071 flow histories revealed by carbonate clumped isotopes ( $\Delta 47$ )—Middle Jurassic  
1072 carbonates of the Paris Basin depocentre. *Sedimentology* 65, 123–150.
- 1073 Manning, C.E., 2014. A piece of the deep carbon puzzle. *Nat. Geosci.* 7, 333–334.
- 1074 Manning, C.E., Shock, E.L., Sverjensky, D.A., 2013. The chemistry of carbon in aqueous fluids  
1075 at crustal and upper-mantle conditions: experimental and theoretical constraints. *Rev.*  
1076 *Mineral. Geochem.* 75, 109–148.
- 1077 Martin, C., Flores, K.E., Vitale Brovarone, A., Angiboust, S., Harlow, G.E., 2020. Deep mantle  
1078 serpentinization in subduction zones: Insight from in situ B isotopes in slab and mantle  
1079 wedge serpentinites. *Chem. Geol.* 545, 119637.
- 1080 Martini, A.M., Walter, L.M., McIntosh, J.C., 2008. Identification of microbial and thermogenic  
1081 gas components from Upper Devonian black shale cores, Illinois and Michigan basins.  
1082 *Aapg Bull.* 92, 327–339.
- 1083 Ménez, B., Pisapia, C., Andreani, M., Jamme, F., Vanbellinghen, Q.P., Brunelle, A., Richard,  
1084 L., Dumas, P., Réfrégiers, M., 2018. Abiotic synthesis of amino acids in the recesses of  
1085 the oceanic lithosphere. *Nature* 564, 59–63. [https://doi.org/10.1038/s41586-018-0684-](https://doi.org/10.1038/s41586-018-0684-z)  
1086 [z](https://doi.org/10.1038/s41586-018-0684-z)
- 1087 Ono, S., Rhim, J.H., Gruen, D.S., Taubner, H., Kölling, M., Wegener, G., 2021. Clumped  
1088 isotopologue fractionation by microbial cultures performing the anaerobic oxidation of  
1089 methane. *Geochim. Cosmochim. Acta* 293, 70–85.
- 1090 Peltola, E., 1968. On some geochemical features in the black schists of the Outokumpu area,  
1091 Finland. *Bull Geol Soc Finl.* 40, 39–50.
- 1092 Peng, W., Tumati, S., Zhang, L., Tiraboschi, C., Vitale Brovarone, A., Toffolo, L., Poli, S.,  
1093 2022. An Experimental Study on Kinetics-Controlled Ca-Carbonate Aqueous  
1094 Reduction into CH<sub>4</sub> (1 and 2 GPa, 550° C): Implications for C Mobility in Subduction  
1095 Zones. *J. Petrol.* 63.
- 1096 Peng, W., Zhang, L., Tumati, S., Vitale Brovarone, A., Hu, H., Cai, Y., Shen, T., 2021. Abiotic  
1097 methane generation through reduction of serpentinite-hosted dolomite: implications for  
1098 carbon mobility in subduction zones. *Geochim. Cosmochim. Acta* 311, 119–140.

1099 Philpotts, J.A., Schnetzler, C.C., 1968. Europium anomalies and the genesis of basalt. *Chem.*  
1100 *Geol.* 3, 5–13.

1101 Piccoli, F., Ague, J.J., Chu, X., Tian, M., Vitale Brovarone, A., 2021. Field-based evidence for  
1102 intra-slab high-permeability channel formation at eclogite-facies conditions during  
1103 subduction. *Geochem. Geophys. Geosystems* 22, e2020GC009520.

1104 Piccoli, F., Vitale Brovarone, A., Beyssac, O., Martinez, I., Ague, J.J., Chaduteau, C., 2016.  
1105 Carbonation by fluid–rock interactions at high-pressure conditions: implications for  
1106 carbon cycling in subduction zones. *Earth Planet. Sci. Lett.* 445, 146–159.

1107 Piccoli, F., Vitale Brovarone, A., Ague, J.J., 2018. Field and petrological study of  
1108 metasomatism and high-pressure carbonation from lawsonite eclogite-facies terrains,  
1109 Alpine Corsica. *Lithos* 304–307, 16–37.

1110 Plank, T., Manning, C.E., 2019. Subducting carbon. *Nature* 574, 343–352.

1111 Plümpner, O., King, H.E., Geisler, T., Liu, Y., Pabst, S., Savov, I.P., Rost, D., Zack, T., 2017.  
1112 Subduction zone forearc serpentinites as incubators for deep microbial life. *Proc. Natl.*  
1113 *Acad. Sci.* 114, 4324–4329.

1114 Rumble, D., Duke, E.F., Hoering, T.L., 1986. Hydrothermal graphite in New Hampshire:  
1115 Evidence of carbon mobility during regional metamorphism. *Geology* 14, 452–455.

1116 Saccocia, P.J., Seewald, J.S., Shanks III, W.C., 2009. Oxygen and hydrogen isotope  
1117 fractionation in serpentine–water and talc–water systems from 250 to 450 C, 50 MPa.  
1118 *Geochim. Cosmochim. Acta* 73, 6789–6804.

1119 Scambelluri, M., Bebout, G.E., Belmonte, D., Gilio, M., Campomenosi, N., Collins, N.,  
1120 Crispini, L., 2016. Carbonation of subduction-zone serpentinite (high-pressure  
1121 ophicarbonate; Ligurian Western Alps) and implications for the deep carbon cycling.  
1122 *Earth Planet. Sci. Lett.* 441, 155–166.

1123 Schrenk, M.O., Brazelton, W.J., Lang, S.Q., 2013. Serpentinization, carbon, and deep life. *Rev.*  
1124 *Mineral. Geochem.* 75, 575–606.

1125 Schulte, M., Blake, D., Hoehler, T., McCOLLUM, T., 2006. Serpentinization and its  
1126 implications for life on the early Earth and Mars. *Astrobiology* 6, 364–376.

1127 Schwartz, S., Guillot, S., Reynard, B., Lafay, R., Debret, B., Nicollet, C., Lanari, P., Auzende,  
1128 A.L., 2013. Pressure–temperature estimates of the lizardite/antigorite transition in high  
1129 pressure serpentinites. *Lithos* 178, 197–210.

1130 Schwarzenbach, E.M., Früh-Green, G.L., Bernasconi, S.M., Alt, J.C., Plas, A., 2013.  
1131 Serpentinization and carbon sequestration: A study of two ancient peridotite-hosted  
1132 hydrothermal systems. *Chem. Geol.* 351, 115–133.

1133 Shilobreeva, S., Martinez, I., Busigny, V., Agrinier, P., Laverne, C., 2011. Insights into C and  
1134 H storage in the altered oceanic crust: Results from ODP/IODP Hole 1256D. *Geochim.*  
1135 *Cosmochim. Acta* 75, 2237–2255.

1136 Shuai, Y., Etiope, G., Zhang, S., Douglas, P.M., Huang, L., Eiler, J.M., 2018. Methane clumped  
1137 isotopes in the Songliao Basin (China): New insights into abiotic vs. biotic hydrocarbon  
1138 formation. *Earth Planet. Sci. Lett.* 482, 213–221.

1139 Spandler, C., Hermann, J., Arculus, R., Mavrogenes, J., 2003. Redistribution of trace elements  
1140 during prograde metamorphism from lawsonite blueschist to eclogite facies;  
1141 implications for deep subduction-zone processes. *Contrib. Mineral. Petrol.* 146, 205–  
1142 222.

1143 Spandler, C., Hermann, J., Faure, K., Mavrogenes, J.A., Arculus, R.J., 2008. The importance  
1144 of talc and chlorite “hybrid” rocks for volatile recycling through subduction zones;  
1145 evidence from the high-pressure subduction mélange of New Caledonia. *Contrib.*  
1146 *Mineral. Petrol.* 155, 181–198.

1147 Stewart, E.M., Ague, J.J., Ferry, J.M., Schiffries, C.M., Tao, R.-B., Isson, T.T., Planavsky,  
1148 N.J., 2019. Carbonation and decarbonation reactions: Implications for planetary  
1149 habitability. *Am. Mineral. J. Earth Planet. Mater.* 104, 1369–1380.

1150 Stolper, D.A., Lawson, M., Davis, C.L., Ferreira, A.A., Neto, E.S., Ellis, G.S., Lewan, M.D.,  
1151 Martini, A.M., Tang, Y., Schoell, M., 2014. Formation temperatures of thermogenic  
1152 and biogenic methane. *Science* 344, 1500–1503.

1153 Stolper, D.A., Martini, A.M., Clog, M., Douglas, P.M., Shusta, S.S., Valentine, D.L., Sessions,  
1154 A.L., Eiler, J.M., 2015. Distinguishing and understanding thermogenic and biogenic  
1155 sources of methane using multiply substituted isotopologues. *Geochim. Cosmochim.*  
1156 *Acta* 161, 219–247.

1157 Sverjensky, D., Daniel, I., Vitale Brovarone, A., 2020. The changing character of Carbon in  
1158 fluids with pressure: Organic geochemistry of Earth's upper mantle fluids. *Carbon*  
1159 *Earths Inter.* 259–269.

1160 Tao, R., Zhang, L., Tian, M., Zhu, J., Liu, X., Liu, J., Höfer, H.E., Stagno, V., Fei, Y., 2018.  
1161 Formation of abiotic hydrocarbon from reduction of carbonate in subduction zones:  
1162 Constraints from petrological observation and experimental simulation. *Geochim.*  
1163 *Cosmochim. Acta* 239, 390–408.

1164 Tumiati, S., Recchia, S., Remusat, L., Tiraboschi, C., Sverjensky, D.A., Manning, C.E., Vitale  
1165 Brovarone, A., Boutier, A., Spanu, D., Poli, S., 2022. Subducted organic matter  
1166 buffered by marine carbonate rules the carbon isotopic signature of arc emissions. *Nat.*  
1167 *Commun.* 13, 1–10.

1168 Tumiati, S., Tiraboschi, C., Miozzi, F., Vitale Brovarone, A., Manning, C.E., Sverjensky, D.A.,  
1169 Milani, S., Poli, S., 2020. Dissolution susceptibility of glass-like carbon versus  
1170 crystalline graphite in high-pressure aqueous fluids and implications for the behavior  
1171 of organic matter in subduction zones. *Geochim. Cosmochim. Acta* 273, 383–402.

1172 Valley, J.W., 1986. Stable isotope geochemistry of metamorphic rocks. *Rev. Mineral.*  
1173 *Geochem.* 16, 445–489.

1174 Van Baalen, M.R., Mossman, B.T., Gunter, M.E., Francis, C.A., 2009. Environmental Geology  
1175 of Belvidere Mt. Guideb, Guidebook for Field Trips in the Northeast Kingdom of  
1176 Vermont and Adjacent Regions, Westerman, D.S. and Lathrop, A.S., eds., The New  
1177 England Intercollegiate Geological Conference, 101st Annual Meeting, Lyndonville,  
1178 Vermont. pp. 71-93.

1179 Vitale Brovarone, A., Martinez, I., Elmaleh, A., Compagnoni, R., Chaduteau, C., Ferraris, C.,  
1180 Esteve, I., 2017. Massive production of abiotic methane during subduction evidenced  
1181 in metamorphosed ophicarbonates from the Italian Alps. *Nat. Commun.* 8, 14134.

1182 Vitale Brovarone, A., Sverjensky, D.A., Piccoli, F., Ressico, F., Giovannelli, D., Daniel, I.,  
1183 2020a. Subduction hides high-pressure sources of energy that may feed the deep  
1184 subsurface biosphere. *Nat. Commun.* 11, 1–11.

1185 Vitale Brovarone, A., Tumiati, S., Piccoli, F., Ague, J.J., Connolly, J.A., Beyssac, O., 2020b.  
1186 Fluid-mediated selective dissolution of subducting carbonaceous material: Implications  
1187 for carbon recycling and fluid fluxes at forearc depths. *Chem. Geol.* 549, 119682.

1188 Wenner, D.B., Taylor, H.P., 1971. Temperatures of serpentinization of ultramafic rocks based  
1189 on  $^{18}\text{O}/^{16}\text{O}$  fractionation between coexisting serpentine and magnetite. *Contrib.*  
1190 *Mineral. Petrol.* 32, 165–185.

1191 Yamaoka, K., Ishikawa, T., Matsubaya, O., Ishiyama, D., Nagaishi, K., Hiroyasu, Y., Chiba,  
1192 H., Kawahata, H., 2012. Boron and oxygen isotope systematics for a complete section  
1193 of oceanic crustal rocks in the Oman ophiolite. *Geochim. Cosmochim. Acta* 84, 543–  
1194 559.

1195 Young, E.D., Kohl, I.E., Lollar, B.S., Etiope, G., Rumble, D., Li, S., Haghnegahdar, M.A.,  
1196 Schauble, E.A., McCain, K.A., Foustoukos, D.I., 2017. The relative abundances of

1197 resolved  $^{12}\text{CH}_2\text{D}_2$  and  $^{13}\text{CH}_3\text{D}$  and mechanisms controlling isotopic bond ordering in  
 1198 abiotic and biotic methane gases. *Geochim. Cosmochim. Acta* 203, 235–264.  
 1199 Zhang, S., Ague, J.J., Vitale Brovarone, A., 2018. Degassing of organic carbon during regional  
 1200 metamorphism of pelites, Wepawaug Schist, Connecticut, USA. *Chem. Geol.* 490, 30–  
 1201 44.  
 1202 Zheng, Y.-F., 1999. Oxygen isotope fractionation in carbonate and sulfate minerals. *Geochem.*  
 1203 *J.* 33, 109–126.  
 1204 Zheng, Y.-F., 1993. Calculation of oxygen isotope fractionation in hydroxyl-bearing silicates.  
 1205 *Earth Planet. Sci. Lett.* 120, 247–263.  
 1206

1207

## Figures captions

**Fig. 1:** A: Simplified geological map of Northeast Vermont, modified from Hibbard et al., (2006). B: Simplified bedrock geologic map of the Belvidere Mountain Complex and the surrounding formations. Modified after Hibbard et al., (2006). Unit descriptions from Hibbard et al. (2006) and Gale (2007).

**Fig. 2:** A-B: Field occurrence of graphite zone A (A). The graphite-enriched shear zone (B) is present inside serpentinized peridotites. C: Carbonate and magnetite veins located on the sides of graphite zone A. D: Graphite zone B. The wall shown in the picture is a graphite-enriched slip plane marking the boundary between amphibolites and serpentinized peridotites. The graphite enrichment can be observed within about 3 meters inside the amphibolite. E: Albite-carbonate veins cutting across the outer margin of the amphibolite next to graphite zone B. The host amphibolite is here intensely affected by greenschist-facies overprinting. F: Example of rodingite-like metasomatism locally affecting the outer portion of the amphibolite at graphite zone B. Gt: garnet; Ep: epidote; Cc: calcite.

**Fig. 3:** Map showing the geology, sample location,  $\delta^{13}\text{C}$  (‰ VPDB), of organic carbon content (wt.%), and  $^{87}\text{Sr}/^{86}\text{Sr}$  ratio results. Pie charts indicate the relative composition of different phases in fluid inclusion as determined from Micro-Raman spectra following the method by Frezzotti et al. (2012). The initial presence of water in olivine-hosted fluid inclusions is deduced from the presence of hydrated step daughter minerals. See Fig. 4 for details on graphite zone A.

**Fig. 4:** Field view details of graphite zone A. The location of the studied samples and associated values of  $\delta^{13}\text{C}$  ‰ (VPDB), wt.% of organic carbon and  $^{87}\text{Sr}/^{86}\text{Sr}$  ratios are also shown. The black-colored area represents the location of the graphite-rich shear zone. The shaded yellow-colored area indicates the carbonate-enriched selvages next to the graphite zone. Thin section scans are also shown in order to highlight the distribution of graphite (dark samples) with respect to the enclosing graphite-free ultramafic rocks.

**Fig. 5:** Photomicrographs of graphite zone A. A: Sample V18-5i from graphite zone A. Pervasive carbonate veins are crosscutting the host antigorite + graphite rock. B: Samples V18-5c from graphite zone A. Fine-grained tremolite is replaced by larger tremolite crystals. The tremolite-rich rock has been partially replaced by antigorite. Graphite appears inside antigorite clast and at the rim of tremolite crystals. C: Sample at the edge of graphite zone A (V18-5a). Tremolite crystals have been replaced by antigorite, with graphite rims outlining the pseudomorphic texture. D: SEM backscattered electron image of sample V18-7c. Carbonate reduction is suggested by the transformation of dolomite to calcite + brucite + graphite. E: Clasts of antigorite in a foliated matrix of fine grained tremolite from graphite zone A (V18-Y1). The tremolite foliation is overgrown by static diopside porphyroblasts. F: Edge of an antigorite-rich clast in contact with tremolite matrix (V18-Yb). In this case, the presence of graphite along the edges to tremolite crystals suggest that the graphite precipitation occurred after the serpentinite brecciation and tremolite precipitation in vein (cf. E). with graphite deposit associated with graphite zone A. Atg: antigorite,

1252 Trm: tremolite, Di: diopside, G: graphite, Chl: chlorite, Cc: calcite, Dol, dolomite, Br:  
1253 brucite.

1254 **Fig. 6:** Photomicrographs of graphite zone B. A: Tremolite-graphite assemblage  
1255 (V18-12a), analogous to samples observed in graphite zone A. B: Graphite rimming  
1256 epidote and titanite crystals inside the edge of the amphibolite at graphite zone B  
1257 (V18-12c). C-D: Brittle deformation inside albite-carbonate veins (V18-14). Note that  
1258 clasts of albite crystals are sealed by carbonate. Graphite preferentially forms along  
1259 pressure-solution domains at albite-carbonate boundaries (D; SEM backscattered  
1260 electron image). Graphite is associated with carbonate. G: graphite, Trm: tremolite,  
1261 Amph: amphibole, Ttn: titanite, Bt: biotite, Ab: albite, Cc: calcite.

1262 **Fig. 7:** A: Isotopic compositions of the main carbon bearing objects in the BMC.  
1263 Error bars do not appear when comprised within the symbol size.

1264 **Fig. 8:** A: Inverse of organic carbon concentration versus  $\delta^{13}\text{C}_{\text{org}}$  composition of  
1265 BMC samples. B:  $\delta^{11}\text{B}$  value versus  $^{87}\text{Sr}/^{86}\text{Sr}$  ratio with data. Boron data from Martin  
1266 et al., (2020) and strontium data from Cannaò et al., (2016) (Cima di Gagnone) and  
1267 Yamaoka et al., (2012) (Oman ophiolite). Metasediment (V18-1a) age corrected at  
1268 300 Ma. DM: depleted Mantle.

1269 **Fig. 9:** Carbonate  $\delta^{13}\text{C}$  and  $\delta^{18}\text{O}$  Isotopic compositions from the BMC. Indicative  
1270 proximities to the graphite zones indicated below samples' name. Reactional trend  
1271 associated with formation of  $\text{CO}_2$  from prograde decarbonation (blue), and carbonate  
1272 reduction (green) from Piccoli et al. (2018) and Debret et al. (2015).

1273 **Fig. 10:** A: Ranges of  $\delta^{13}\text{C}$  and  $\delta^2\text{H}$  measured in methane-rich fluid inclusions. A  
1274 variety of sources are displayed as references from Bradley and Summons (2010).  
1275 'Autotrophic' refers to methane produced by  $\text{H}_2/\text{CO}_2$  methanogenesis, while  
1276 'heterotrophic' refers to methane produced by fermentation of acetate or  
1277 consumption of methylated organic compounds. 'Thermogenic' refers to cracking of  
1278 biologically derived oils, while 'geothermal' refers to cracking of high-molecular-  
1279 weight organic compounds. B:  $\delta^2\text{H}$  values of  $\text{CH}_4$  and  $\text{H}_2$  from fluid inclusions.  
1280 Methane and hydrogen produced by activity of methanogens are expected to fall  
1281 within the grey box and additional reference data from Bradley and Summons,  
1282 (2010).

1283 **Fig. 11:** Modeling of equilibrium fractionation for methanation of calcite at 450 °C. A  
1284 calcite with an initial  $\delta^{13}\text{C}$  isotopic composition of -8 ‰ is considered, using  
1285 fractionation factor from Bottinga (1969).

1286 **Fig. 12:** Modeling at 450°C and 1.1 GPa of the desiccation of a fluid near water  
1287 maximum toward reducing conditions fluid with an isotopic composition of  $\delta^{13}\text{C}=-45$   
1288 ‰ (A-E), and modeling of the mixing of a slightly reduced fluid with an isotopic  
1289 composition of  $\delta^{13}\text{C}=-45$  ‰ and a reduced fluid with an isotopic composition of  
1290  $\delta^{13}\text{C}=-23$  ‰ (F-J). A and F: zoom on a COH diagram of the initial and final position  
1291 of the involved fluids. B and G: evolution of the  $\text{CH}_4/(\text{CH}_4+\text{CO}_2)$  ratio and of the  
1292  $\text{H}_2\text{O}/(\text{CH}_4+\text{CO}_2+\text{H}_2\text{O})$  ratio during the modeled fluid interactions. C and H: evolution  
1293 of the oxygen fugacity of the fluid during the modeled fluid interactions. D and I:



evolution of the total amount of graphite in mole in the system during the modeled fluid interactions. *E and J*: evolution of the isotopic composition of the main carbon bearing species in the system during the modeled fluid interaction. The model does a titration of one fluid in another and tracks the carbon activity of the system according to equation from Huizenga (2004). New graphite composition corresponds to the instantaneous composition of graphite precipitating while total graphite account for the global composition of graphite in the system.

**Fig. 13:** Proposed model of BMC hydration in subduction zone associated with graphite deposition linked to CH<sub>4</sub> migration. *A*: Initial stage of the BMC in subduction, graphite zone A corresponds to a shear zone and graphite zone B to the lithologic contact with the amphibolite. *B*: Infiltration of a fluid from metasedimentary rocks. This fluid was H<sub>2</sub>O dominated, rich in Ca, Si, C, and N, and produced tremolite metasomatism along the main fluid channels. *C*: CH<sub>4</sub> released from serpentinization escapes along main fluid channel and precipitates graphite when encountering redox barrier. *D*: As the CH<sub>4</sub> production and escape progresses, the CH<sub>4</sub> becomes dominant across the study zone and the redox front progresses in the amphibolite.

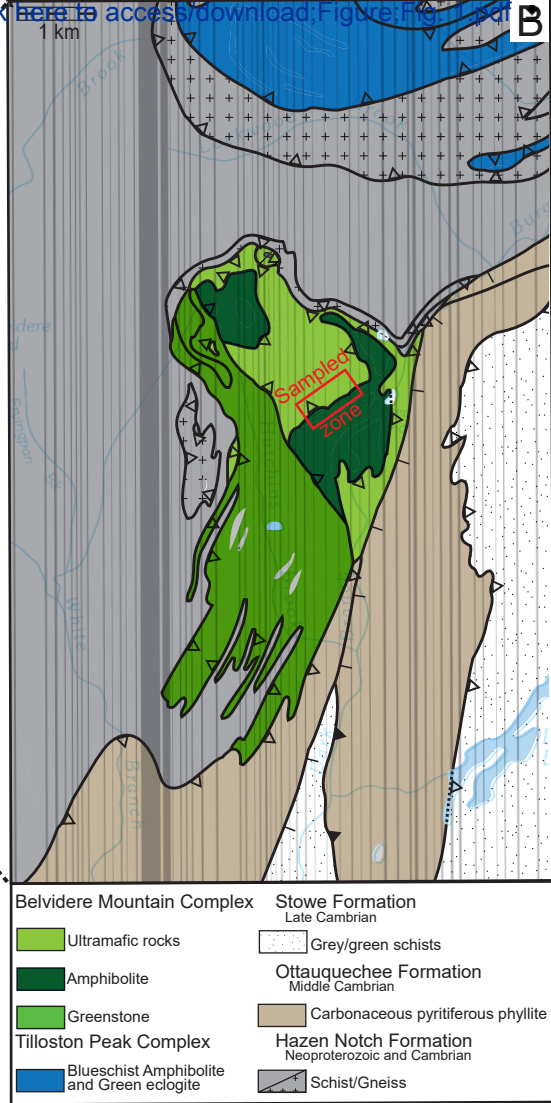
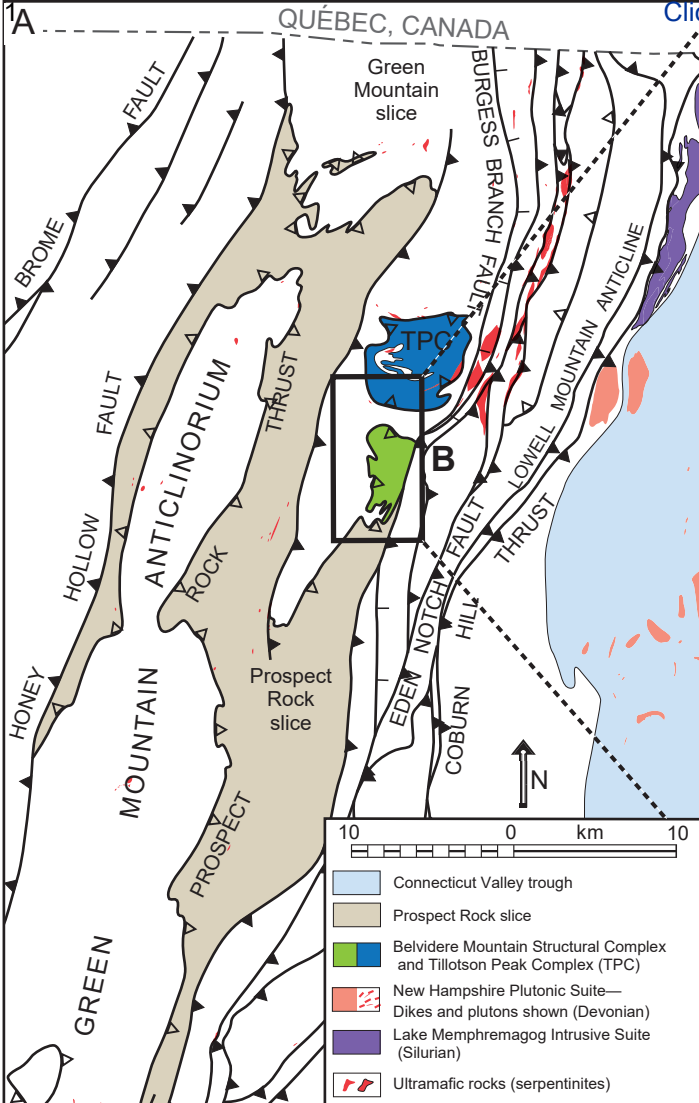
Table captions

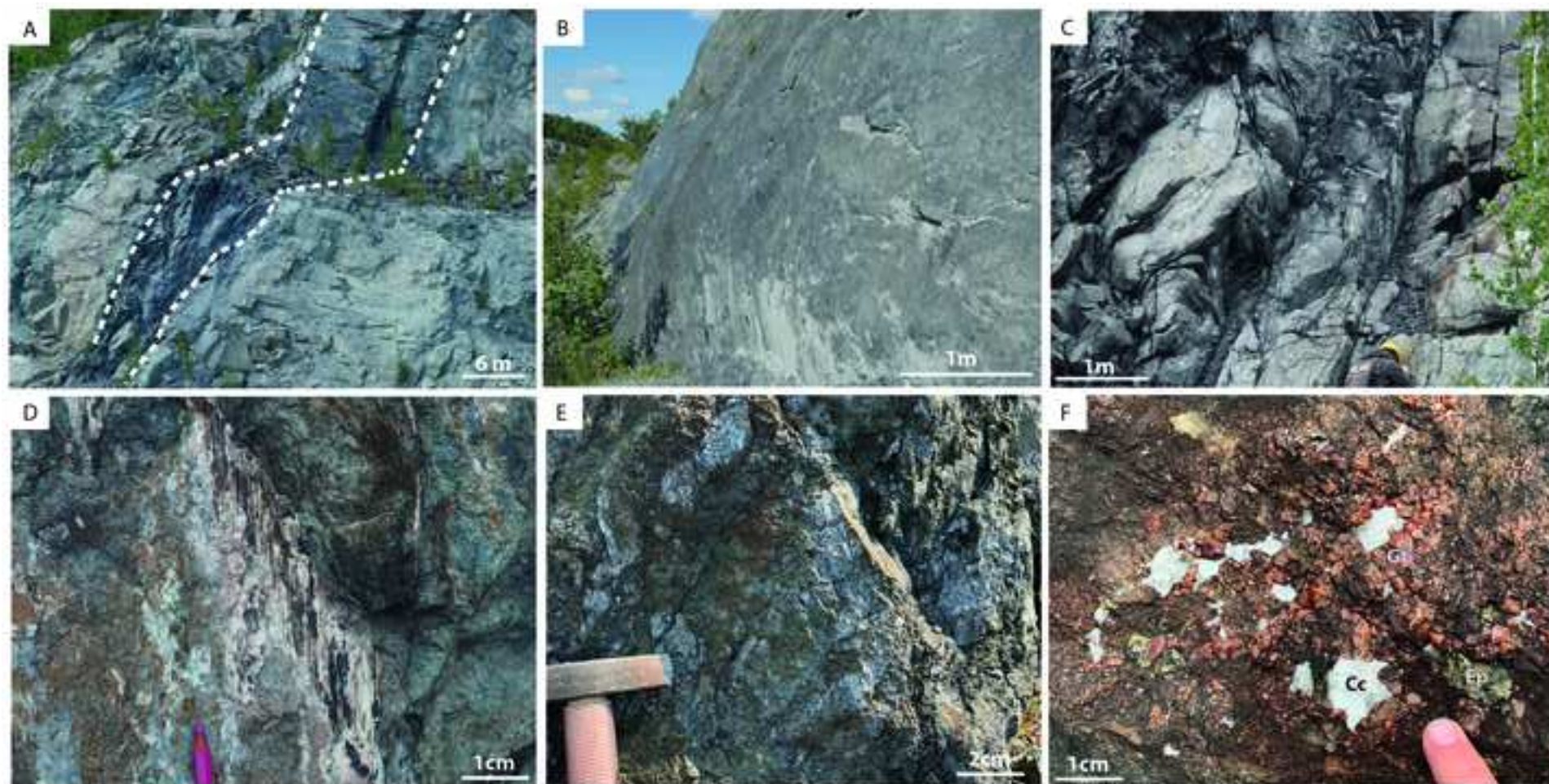
**Table 1:** Studied BMC samples and related carbon, strontium and boron data.

**Table 1:** Studied BMC samples and related carbon, strontium and boron data.

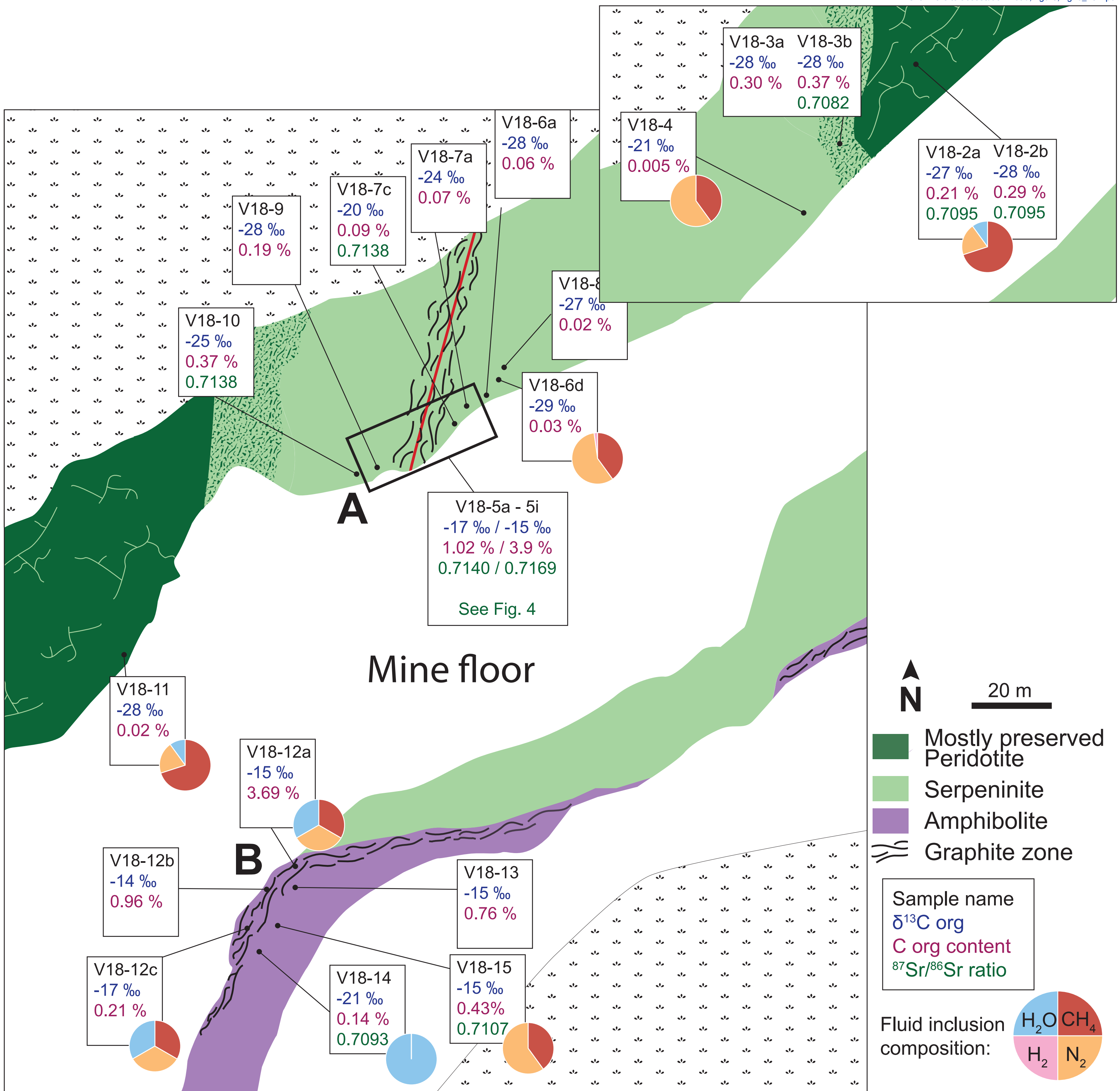
Samples		$C_{org}$	$\delta^{13}C_{org}$	$\delta^{13}C_{inorg}$	$\delta^{18}O_{carbonate}$	$\delta^{13}C_{CH_4}$
		(wt%)	VPDP	VPDP	VSMOW	VPDP picarro
V18-1a		0.58	-25.3			-46.28
V18-1c	metasedimentary rocks	0.17	-25			
V18-1e		1.99	-25			
V18-2a		0.02	-27.4			-12.66
V18-2b	mostly preserved peridotite	0.03	-28.3			
V18-3a		0.03	-28.1			
V18-3b		0.03	-28.5			
V18-4	rodingites	0.01	-21.7			-15.48
V18-Y1						
V18-Yb						
V18-5a		1.39	-15.5			
V18-5b		1.65	-15.2			
V18-5c		1.51	-15.6			
V18-5d	graphite zone A	1.08	-14.6			
V18-5e		1.03	-17			
V18-5f		3.91	-15.3			
V18-5g		2.76	-15.6			
V18-5h		1.45	-16.5			
V18-5i		1.02	-17.7	-1.43	16.64	
V18-6a		0.06	-28.6	-6.49	8.91	
V18-6d		0.03	-29.5			-31.25
V18-7a	serpentinite with variable	0.07	-24.7			
V18-7c	amount of carbonate	0.09	-20.2	-1.27	15.15	
V18-8		0.02	-27.7	-4.5	10.83	
V18-9		0.02	-27.9	-4.13	11.81	
V18-10		0.37	-25.1			
V18-11	mostly preserved peridotite	0.02	-27.7			-45.23
V18-12a		3.69	-15.5			-22.36
V18-12b	graphite zone B	0.96	-13.6			
V18-12c		0.22	-16.9			-18.59
V18-13	amphibolite	0.77	-14.8			
V18-14		0.14	-20.5	-7.26	11.41	-36.95
V18-15	amphibolite with carbonate	0.43	-15.4			-20.19

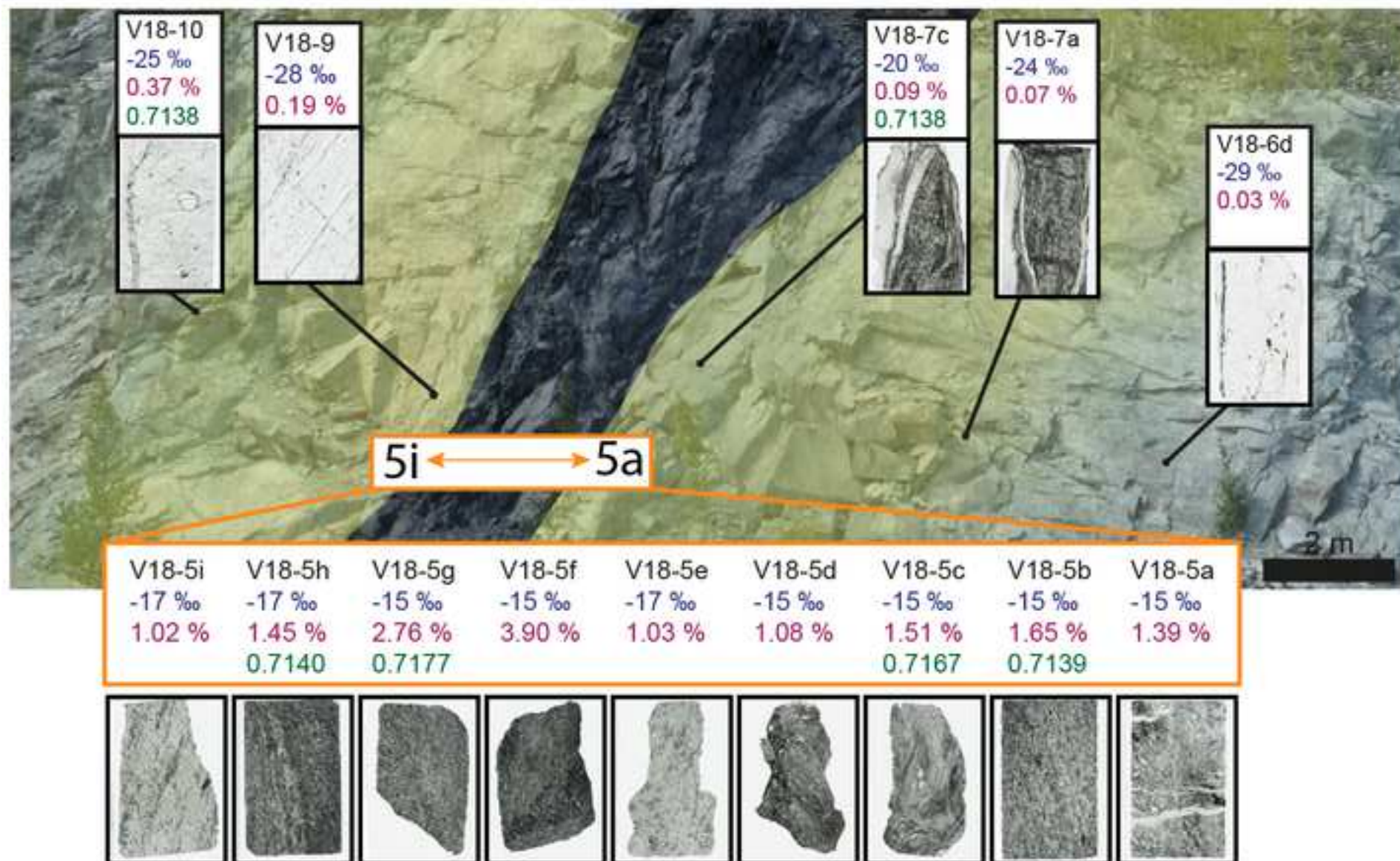
$\delta^{13}\text{C}_{\text{CH}_4}$	$\delta^2\text{H}_{\text{CH}_4}$	$\delta^2\text{H}_{\text{H}_2}$	C1/C2	$^{87}\text{Sr}/^{86}\text{Sr}$	$\delta^{11}\text{B}$
VPDP	VSMOW	VSMOW			
IRMS					
-46.34	-226	-812	13	0.75779	-8.5
-12.93	-171		1992	0.70954	-1.6
				0.7095	-0.8
				0.70822	-1.4
-17.88	-177		6154		
				0.71495	
				0.7167	-3.6
				0.71767	
				0.71401	
-29			635		
				0.71381	-2.4
				0.71381	-4.6
-42.48	-226		668		
-22.46	-161				
-20.66	-140	-680			
-33.45	-168			0.70934	-3.5
-20.18	-168			0.7107	



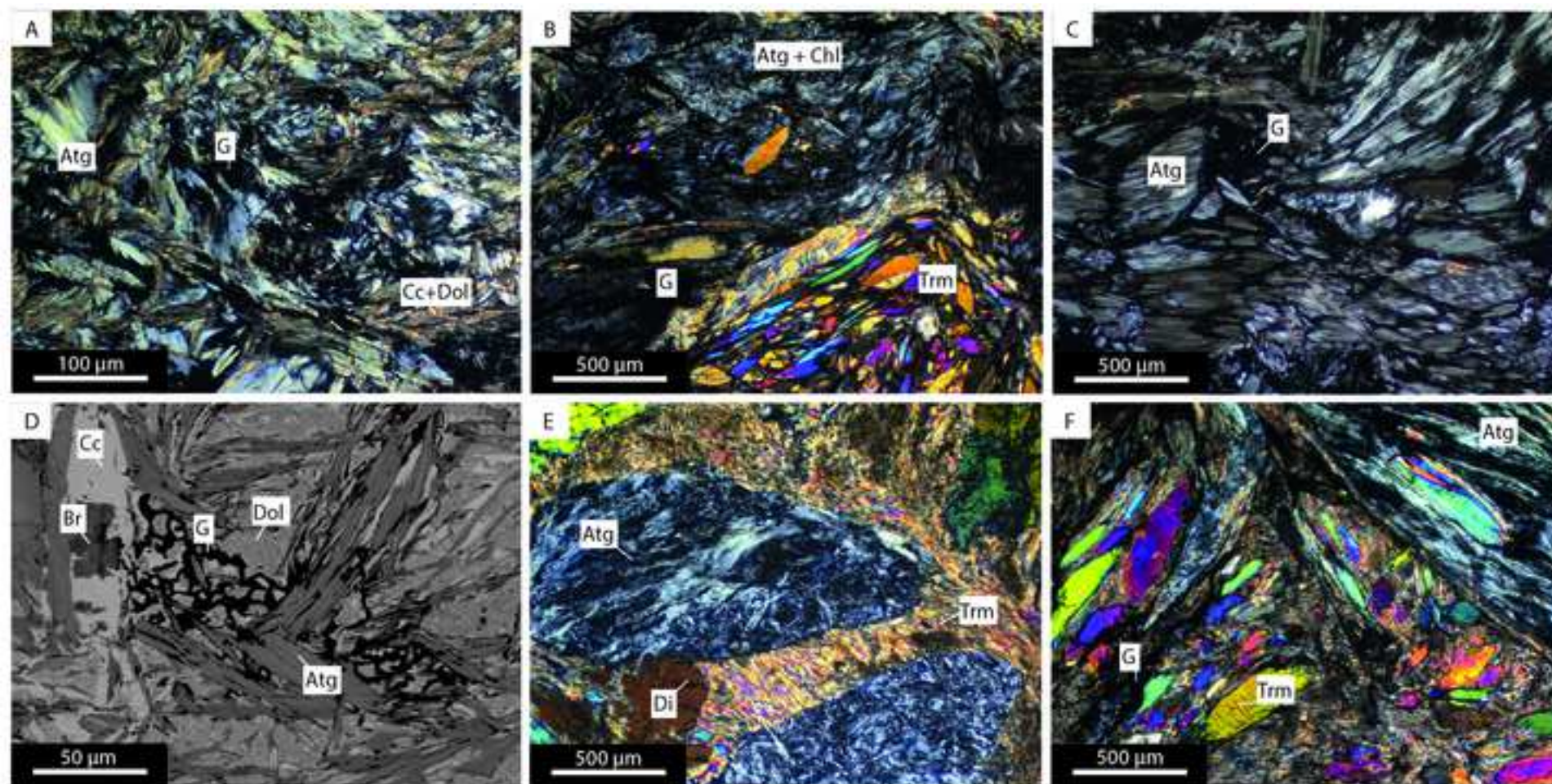




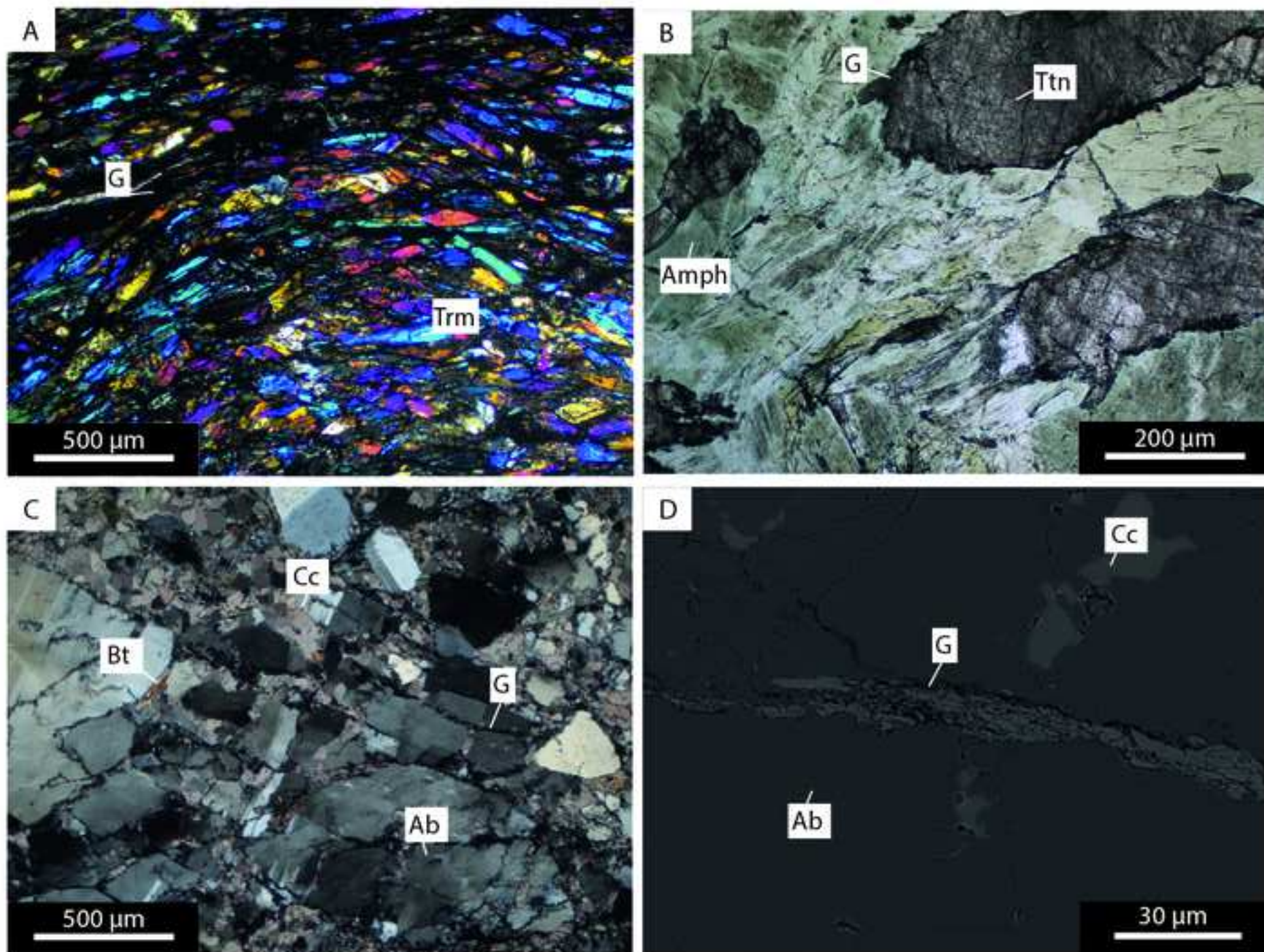


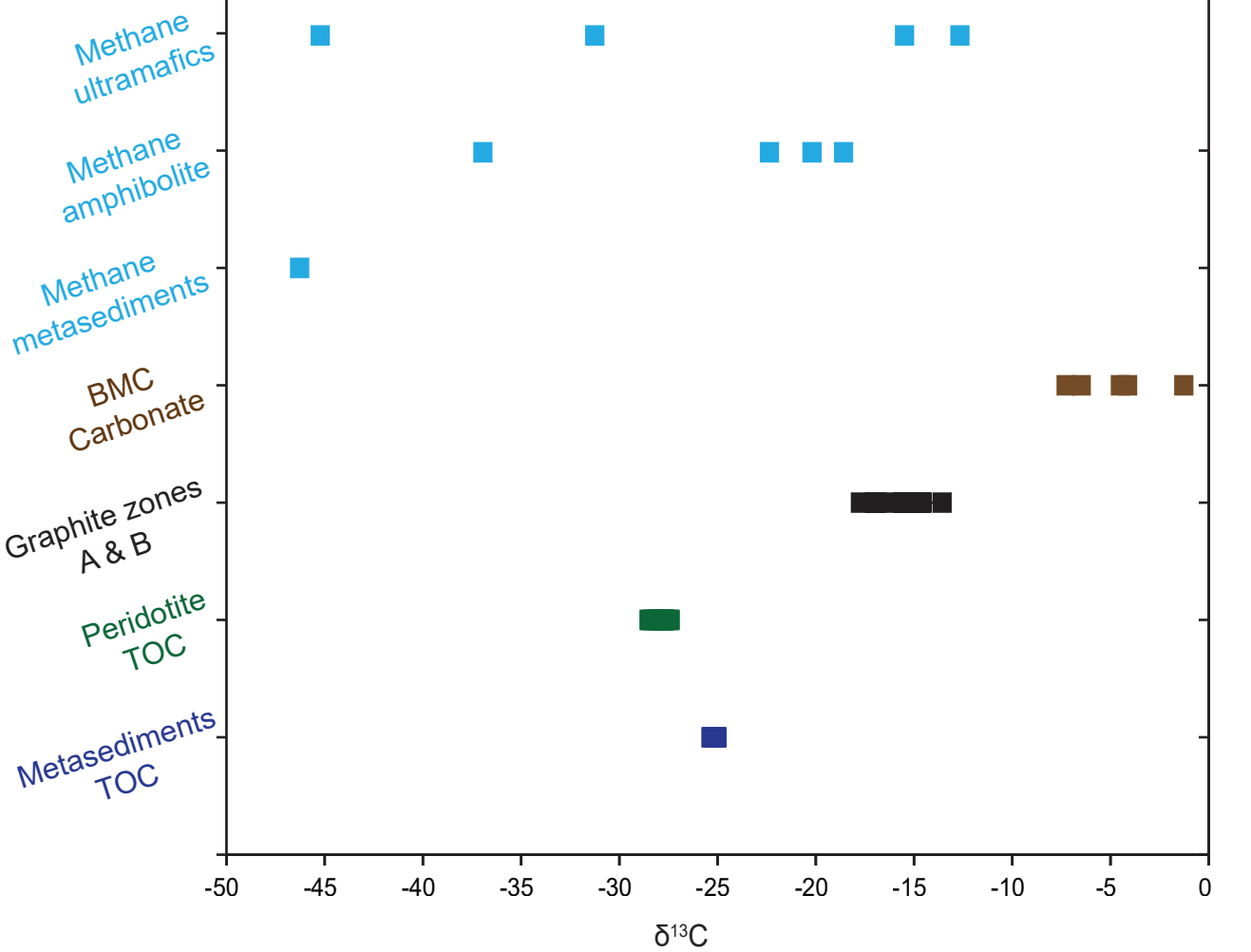


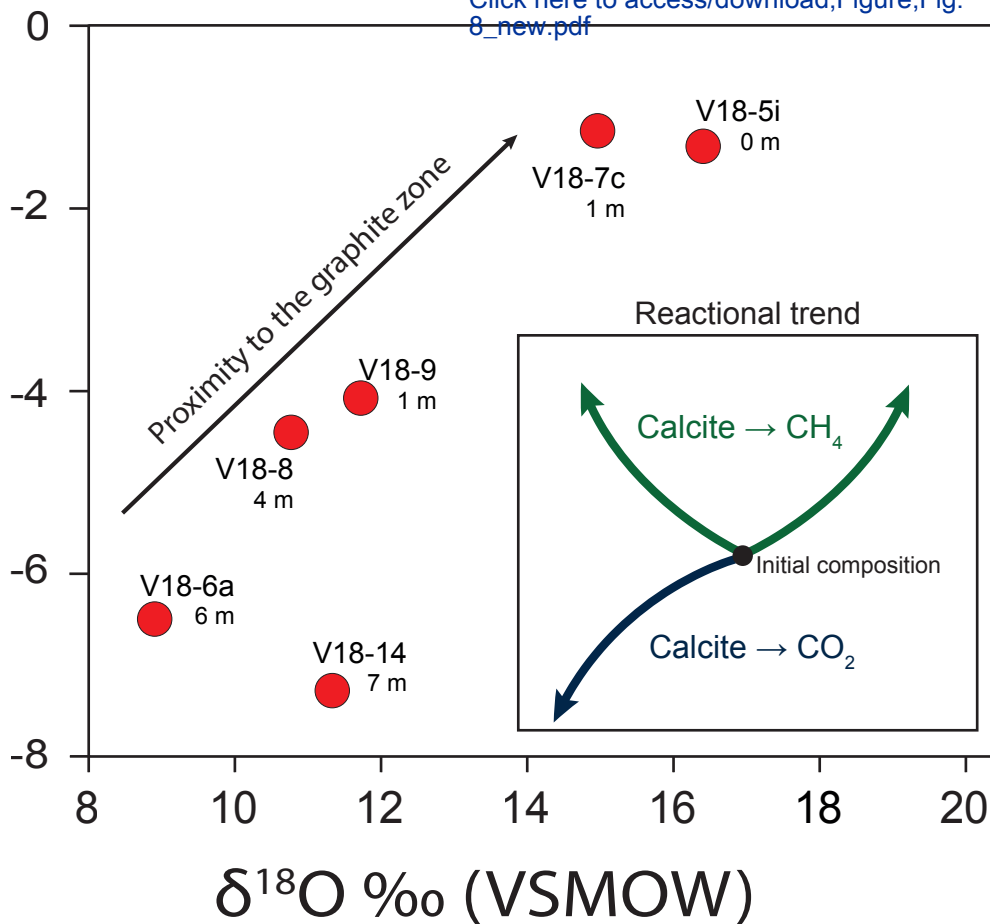




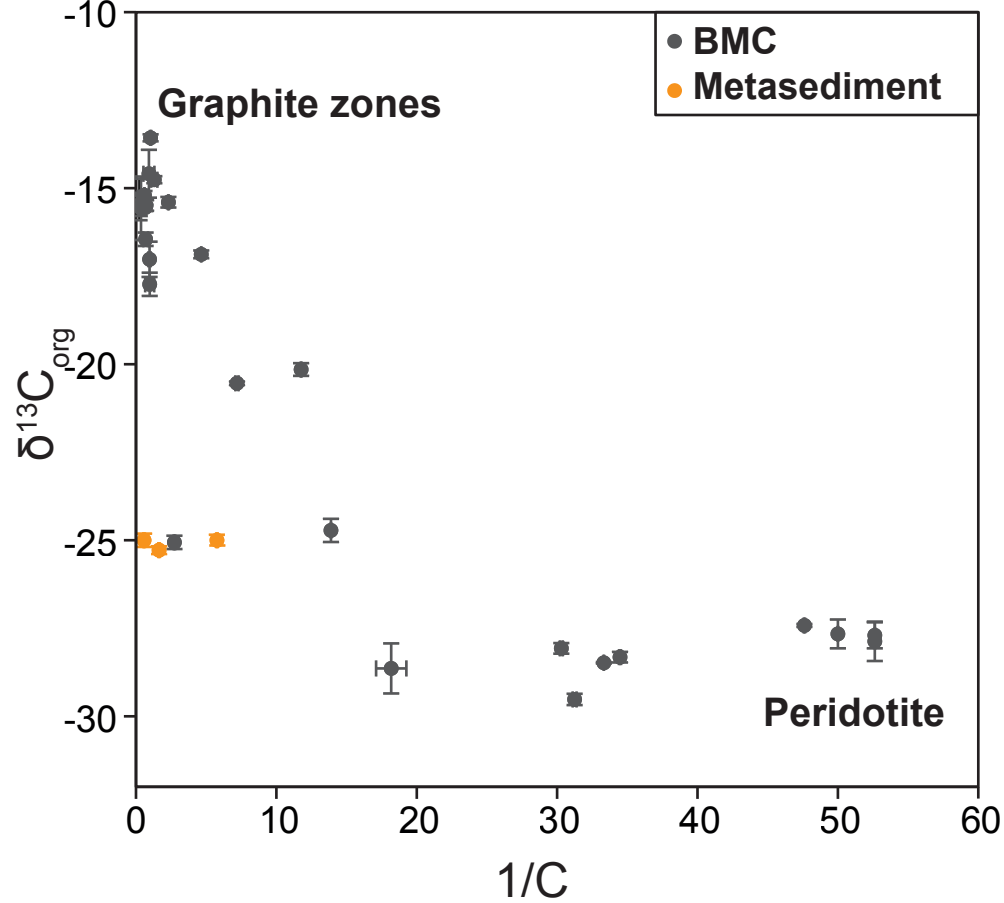






$\delta^{13}\text{C} \text{ ‰ (VPDB)}$ 

9  
A



B

